AGU PUBLICATIONS

JGR

Journal of Geophysical Research: Planets

RESEARCH ARTICLE
10.1002/2013JE004396

Key Points:
- We study two suites of fresh shallow valleys in disparate locations on Mars
- Many (more than tens of) channels travel uphill demanding formation beneath ice cover
- Valley ages are indistinguishable and likely Late Amazonian

Supporting Information:
- Supplemental Figures S1–S5

Correspondence to:
Daniel E. J. Hobley,
daniel.hobley@colorado.edu

Citation:
Hobley, D. E. J., A. D. Howard, and J. M. Moore (2014), Fresh shallow valleys in the Martian midlatitudes as features formed by meltwater flow beneath ice, *J. Geophys. Res. Planets*, *119*, 128–153, doi:10.1002/2013JE004396.

Received 15 MAR 2013
Accepted 21 DEC 2013
Accepted article online 2 JAN 2014
Published online 27 JAN 2014

Fresh shallow valleys in the Martian midlatitudes as features formed by meltwater flow beneath ice

Daniel E. J. Hobley[1,2], Alan D. Howard[2], and Jeffrey M. Moore[3]

[1]Department of Geological Sciences, University of Colorado Boulder, Boulder, Colorado, USA, [2]Department of Environmental Sciences, University of Virginia, Charlottesville, Virginia, USA, [3]NASA Ames Research Center, Moffett Field, California, USA

Abstract Significant numbers of valleys have been identified in the Martian midlatitudes (30–60°N/S), spatially associated with extant or recent ice accumulations. Many of these valleys date to the Amazonian, but their formation during these cold, dry epochs is problematic. In this study, we look in detail at the form, distribution, and quantitative geomorphology of two suites of these valleys and their associated landforms in order to better constrain the processes of their formation. Since the valleys themselves are so young and thus well preserved, uniquely, we can constrain valley widths and courses and link these to the topography from the Mars Orbiter Laser Altimeter and High-Resolution Stereo Camera data. We show that the valleys are both qualitatively and quantitatively very similar, despite their being >5000 km apart in different hemispheres and around 7 km apart in elevation. Buffered crater counting indicates that the ages of these networks are statistically identical, probably forming during the Late Amazonian, ~100 Ma. In both localities, at least tens of valleys cross local drainage divides, apparently flowing uphill. We interpret these uphill reaches to be characteristic of flow occurring beneath a now absent, relatively thin (order 10^1–10^2 m), regionally extensive ice cover. Ridges and mounds occasionally found at the foot of these valley systems are analogous to eskers and aufeis-like refreezing features. On the basis of their interaction with these aufeis-like mounds, we suggest that this suite of landforms may have formed in a single, short episode (perhaps order of days), probably forced by global climate change.

1. Introduction

It is now widely accepted that liquid water has flowed across the surface of Mars at various times in its past [*Craddock and Howard*, 2002; *Malin and Edgett*, 2003]. Much previous research has focused on the large-scale Noachian-era valley networks and later outflow channels, concentrated around the planet's equatorial latitudes [e.g., *Sharp and Malin*, 1975; *Pieri*, 1980; *Phillips et al.*, 2001; *Craddock and Howard*, 2002; *Fassett and Head*, 2008]. However, a growing body of recent work has identified significant numbers of channels and valleys that are much younger, smaller, and better preserved than these older features. These valleys are more prevalent in the midlatitudes [e.g., *Berman et al.*, 2009; *Dickson et al.*, 2009; *Morgan and Head*, 2009; *Fassett et al.*, 2010; *Howard and Moore*, 2011; *Jones et al.*, 2011; *Mangold*, 2012], although they occur locally in equatorial latitudes [*Gulick*, 2001; *Fassett and Head*, 2005; 2006; 2007; *Irwin et al.*, 2005; *Moore et al.*, 2012]. These are distinguished from gullies [*Malin and Edgett*, 2000] by their lack of a well-defined source area, lower gradients, and in general larger widths and lengths [*Fassett et al.*, 2010].

Previous studies have almost always linked the formation of these fresh shallow valleys (FSVs) with ice or snowmelt processes. This is unsurprising since they are mainly found in the bands 30–60°N/S where other ice-mediated surface processes are also concentrated, such as viscous flow features [e.g., *Milliken et al.*, 2003], lobate debris aprons [e.g., *Squyres*, 1979], lobate crater ejecta [e.g., *Barlow and Bradley*, 1990], dissected mantle terrain [e.g., *Mustard et al.*, 2001; *Head et al.*, 2003], concentric crater fills [e.g., *Squyres and Carr*, 1986], gullies [e.g., *Malin and Edgett*, 2000], and recurring slope lineae [e.g., *McEwen et al.*, 2011]. They also tend to be spatially associated with viscous flow features (VFFs) at around the crater scale and finer [e.g., *Fassett et al.*, 2010], and their young ages mean they developed during a period of Martian history which is interpreted as dominantly very cold and hyperarid. However, a significant number of different hypotheses have been proposed to describe the flow processes and geomorphic environments in which these valleys formed. These include (a) formation shortly after crater formation by impact heating of icy regolith [e.g., *Morgan and Head*, 2009; *Jones et al.*, 2011; *Mangold*, 2012]; (b) formation by locally increased geothermal heat flow from the subsurface [*Baker*, 1981; *Basilevsky et al.*, 2006]; (c) formation by melting of ice in VFFs, either cut into their

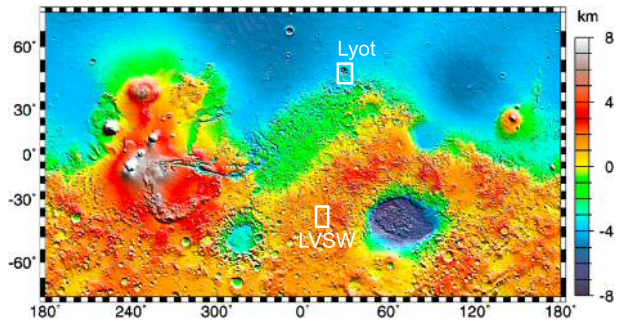

Figure 1. Global topographic map for Mars at 2.5 km resolution derived using MOLA instrument, showing locations of Le Verrier Southwest (LVSW) and Lyot study sites.

tops by surficial ice melt (supraglacial channels), forming immediately adjacent to the ice masses by discharge of subglacial water (proglacial channels), or forming beneath now-vanished ice (subglacial channels) [*Dickson et al*., 2009; *Fassett et al*., 2010]; and (d) formation by snow or ice melt, but favored by both spatially and/or temporarily restricted climatic optima [*Berman et al*., 2009; *Dickson et al*., 2009; *Howard and Moore*, 2011; *Grant and Wilson*, 2012]. Note that these hypotheses are not all mutually exclusive. It remains unclear whether a single suite of contemporaneous processes is responsible for the origin of all of the FSVs, or whether they were formed by different processes at different times in Mars' recent history.

This study aims to critically assess these hypotheses for FSV formation for specific cases by comparison of the form, distribution, and quantitative geomorphology of the valleys and their associated landforms in two distinct study sites. These were selected based on (a) a high density of FSVs for study; (b) availability of acceptable coverage of Context Camera (CTX) imagery; (c) availability of both High-Resolution Stereo Camera (HRSC) and Mars Orbiter Laser Altimeter (MOLA) digital terrain models (DTMs) for the bulk of each locality; (d) existing qualitative interpretation of the features present, both in terms of the valleys but especially the glacial features; and (e) a significant distance between the sites. One site encompasses on a set of craters and their environs immediately southwest of Le Verrier crater and northwest of Kaiser crater in Noachis Terra in the southern highlands, centered around 40.6°S, 13.8°E, which we will term Le Verrier Southwest (LVSW). The other site includes Lyot crater and surroundings, a 220 km diameter, Amazonian [*Greeley and Guest*, 1987] crater north of Deuteronilus Mensae in the northern midlatitudes, centered on 50.4°N, 29.4°E (Figure 1). Both have significant densities of FSVs, previously interpreted to have formed in association with Amazonian glacial features also present in both sites [*Dickson et al*., 2009; *Fassett et al*., 2010]. We have systematically mapped all of the FSVs visible in CTX imagery across these sites, as well as ridges and mounds associated with these valleys. The excellent preservation of the landforms has allowed us to also measure valley widths associated with each FSV. By overlaying these georeferenced CTX swaths onto the HRSC and MOLA terrain models for each area using geographic information system (GIS) software, we have extracted the local slope, elevation, and flow path data for each valley and used these to constrain the relationships between width, bed slope, and drainage structure. These relationships in turn can allow us to discriminate between the various hypotheses for the formation of the FSVs and also to investigate whether the same formation processes could have produced them in each area.

This paper begins by outlining the data used in the study and its processing. We then qualitatively describe the form of the FSVs seen across both areas, and the landforms associated with them, and describe and map their distribution around the landscape. We go on to present quantitatively testable hypotheses for the formation processes creating the FSVs we see, and describe the measurement and crater counting techniques that we use to discriminate between these hypotheses. This is followed by presentation of our data describing the quantitative geomorphology and age of the FSVs and then by a discussion using these data to address the likelihood that these valleys formed beneath a cap of ice and to constrain the environment in which this process may have occurred.

2. Data Acquisition and Handling

Analysis was based on publicly available data sets acquired through the NASA's Planetary Data System. The mapping was conducted using image swaths taken from the Context Camera (CTX) on NASA's Mars Reconnaissance Orbiter satellite. These images have a resolution of 5–7 m/pixel. DTM data were taken both from the High-Resolution Stereo Camera (HRSC) on the European Space Agency's Mars Express satellite and also from the Mars Orbiter Laser Altimeter (MOLA) on board NASA's Mars Global Surveyor spacecraft. In both cases, data were acquired already processed into gridded data (DTM) form.

Each data set was manipulated in the third edition of the Integrated Software for Imagers and Spectrometers (ISIS) software package, provided by the United States Geological Survey. ISIS was used to mosaic different footprints of the CTX and DTM data, to adjust the resolution of the DTM data, and to reproject all the data sets into common spatial projections (Mars sinusoidal, centered at 39.61°S, 11.47°E for LVSW and 48.98°N, 29.18°E for Lyot). These data sets were then loaded into ArcGIS Geographical Information Systems software for mapping and analysis.

Both HRSC and MOLA DTMs are used here, in order both to permit study of the topography of our two sites at different spatial scales and also to reduce the likelihood of systematic error in either data set. MOLA DTMs are constructed by superposing and interpolating between narrow (300 m) strips of data collected by laser altimetry [*Zuber et al*., 1992],and cover the whole surface of Mars at resolutions down to 463 m/pixel. However, these data can suffer from inaccuracies and artifacts in the interpolated zones between strips. In contrast, individual HRSC DTMs are constructed from stereo imagery from a linescan, "push-broom" camera [*Neukum et al*., 2012]. This results in complete spatial coverage within each DTM at higher resolution than MOLA data but over much more spatially restricted areas. The effective resolution of HRSC is variable according to spacecraft height, feature contrast, and atmospheric clarity; in our data, it varied between 75 m/pixel (Lyot) and 250 m/pixel (LVSW). Before beginning the analysis, the two DTMs were cross-correlated to check for internal consistency of our data.

Our CTX, MOLA, and HRSC DTM data are augmented both by a 1 m/pixel DTM built from the High-Resolution Imaging Science Experiment (HiRISE) camera imagery covering a junction between several FSVs in the southwest of Lyot crater (kindly shared with us by Edwin Kite) and by a small number of publicly available HiRISE (~0.5 m/pixel) image tiles. The former allows us to gain some quantitative sense of the depth, and hence aspect ratios, of a very small subset of the studied FSVs, and the latter allows a more detailed assessment of the fine-scale topography of the mapped features in a few areas around the study sites. Due to the strongly restricted spatial coverage of these data types, they do not form a major component of this work. However, we use data drawn from them to support arguments made primarily from our three main data types as presented above.

3. Study Site Landforms

Both sites share a similar suite of landforms. This incorporates both features normally interpreted as ice rich, such as VFFs and dissected mantle terrain (DMT) [see, e.g., *Mustard et al*., 2001; *Head et al*., 2003], and also the FSVs and associated features addressed by this study. We do not set out to here describe the history of landscape evolution in detail for these areas but rather provide short descriptions of key features in the landscape which are associated and interact with the FSVs that are the study focus. We then used these descriptions to systematically map all FSVs and associated ridges, mounds, and fan-like landforms across the CTX imagery, as well as marking the position and extent of VFFs and other ice-rich terrains around the landscape (Figure 2). This map forms the basis for our later analysis of these features (section 6).

3.1. FSV Definition and Morphology

We define a FSV as a shallowly incised, narrow (typically $\ll$500 m), "fresh" valley, with minimal degradation of its sidewalls and often sharp upper edges, as seen in CTX imagery. This freshness strongly suggests that FSVs are post-Noachian structures that have not been exposed to the elevated weathering rates typical of that epoch [*Golombek and Bridges*, 2000] or appreciable subsequent aeolian mantling, mass wasting, or impact gardening [*Hartmann et al*., 2001]. Note that this definition excludes the much larger, wider areal scour features sometimes seen outside and radiating away from the ejecta blankets of young impact structures, for example, around Lyot crater [*Harrison et al*., 2010].

Within this definition, we recognize two end-member types of FSV, which are both found in both localities (Figure 3). We allocate all our mapped FSVs to one of these two categories but emphasize that intermediate examples are found and a continuum of FSV form exists between these end-members.

Type 1. These valleys are very narrow floored, V to slightly U shaped, sharp edged, and tightly sinuous (e.g., Figures 3a and 3b). Valley width is typically $<$50 m. Branching is uncommon, though not unknown. They start and end abruptly, or occasionally join mode 2 FSVs. Very occasionally abandoned flow paths are visible parallel to, but less deeply incised than, the main valley.

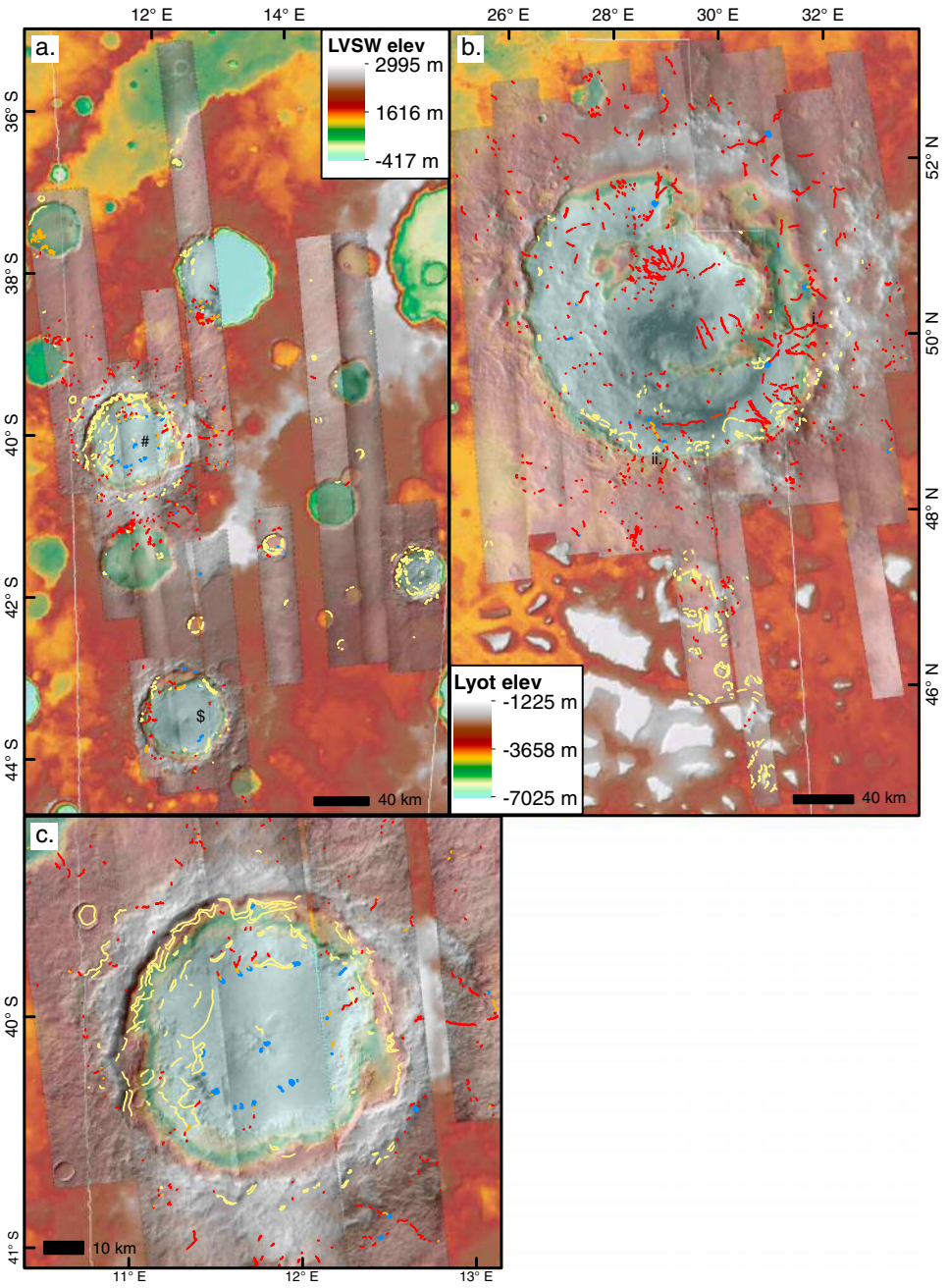

Figure 2. Distribution of mapped FSVs (red), ridges (orange), mounds (blue), and transverse structures within VFFs (yellow) in both study sites. North is up. Mapped features are defined in the main text. CTX tiles used for mapping are shown overlaid onto MOLA DTMs. Widths of linear features are exaggerated for clarity. White lines demark the extent of available HRSC DTMs. In LVSW, HRSC data do not extend west of the line; in Lyot, HRSC data do not extend east of the line. (a) LVSW study site. White is high (max. 2995 m), blue is low (min. −417 m). CTX tiles used are P17_007664_1409_XN_39S349W, P13_005950_1401_XN_39S348W, P15_006807_1391_XN_40S348W, P07_003827_1380_XN_42S348W, P14_006596_1400_XI_40S347W, P13_006240_1419_XN_38S347W, B17_016182_1370_XN_43S347W, B06_011936_1363_XI_43S347W, B18_016749_1368_XN_43S346W, B16_015905_1378_XN_42S345W, P12_005607_1396_XN_40S344W, P15_006886_1396_XN_40S345W, P15_007031_1379_XN_42S343W, and P17_007677_1379_XN_42S343W. (b) Lyot study site. White is high (max. −1225 m), blue is low (min. −7025 m). The dark areas in the crater center and to its south are dune fields, on which FSVs were not observed. CTX tiles used are P03_002270_2303_XN_50N332W, P03_002336_2305_XI_50N333W, P03_002349_2310_XI_51N330W, P03_002415_2310_XI_51N330W, P04_002494_2310_XI_51N328W, P04_002560_2309_XI_50N329W, P04_002626_2304_XI_50N332W, P12_005817_2306_XI_50N330W, P15_006740_2287_XN_48N330W, P15_006819_2296_XN_49N328W, P16_007452_2306_XN_50N331W, P17_007518_2300_XN_50N334W, P17_007821_2306_XN_50N327W, P20_008678_2292_XN_49N330W, P20_008744_2305_XN_50N331W, P21_009179_2308_XI_50N331W, and P22_009825_2316_XN_51N327W. (c) Enlarged view of the crater in LVSW with the highest concentration of FSVs and associated mounds. Note that many (but not all) of the mounds form a ring around the break in slope at the edge of the crater floor and that this is level with the downslope maximum extent of the VFFs.

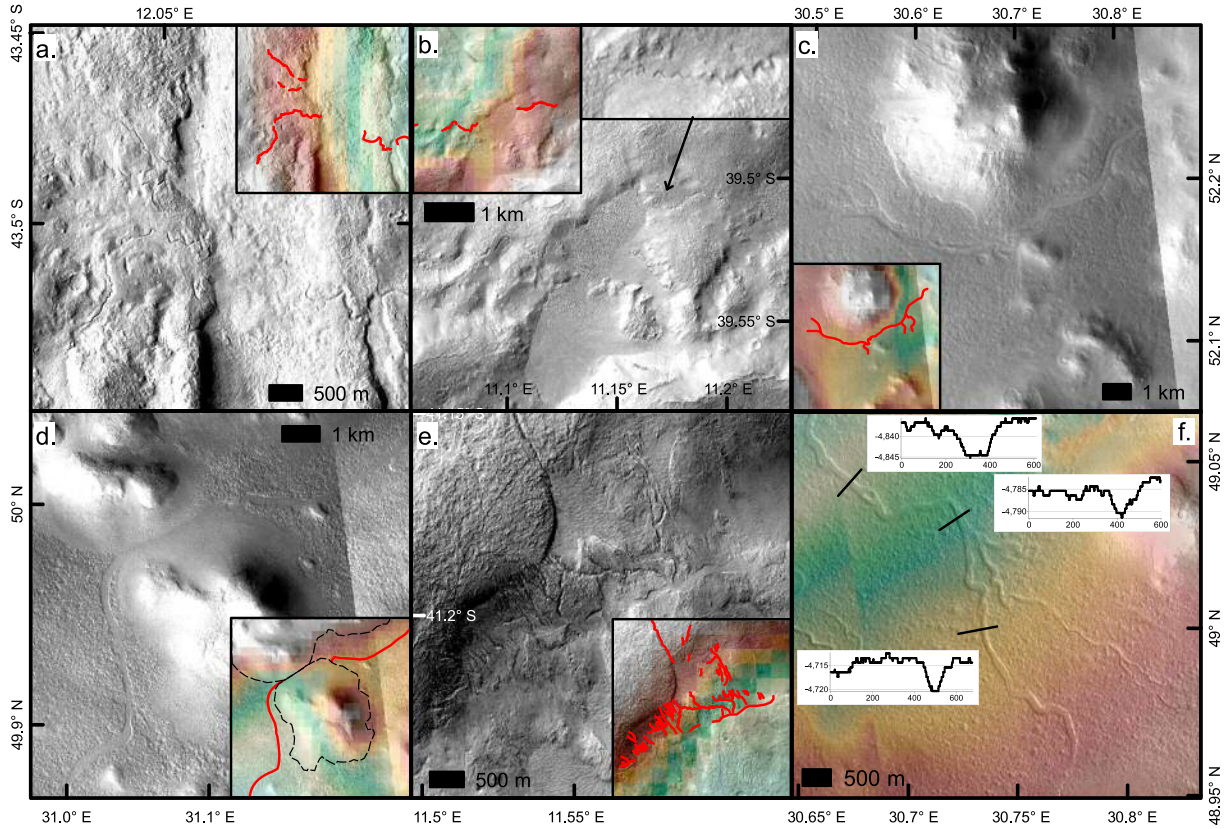

Figure 3. Examples of fresh, shallow valleys (FSVs) from around the study sites. Contrast has been exaggerated to emphasize features. Insets show mapped FSV position and are tinted with relative elevation, following color scheme high to low of white-brown-red-yellow-green-blue. North is up. (a) Type 1 FSVs. Note the high sinuosity and discontinuity. CTX image B06_011936_1363_XI_43S347W. Maximum elevation is 1175 m, minimum is 702 m. (b) Chain of type 1 FSVs. Note tendency of channels to "jump" across local depressions between local highs. The channels are cut into the stratigraphically lowest unit (the "bedrock"). Blowup demonstrates that the FSV shallows and narrows on the sidewall of the depression, but is still present down to the modern DMT surface. CTX image P13_005950_1401_XN_39S348W. Maximum elevation is 2884 m, minimum is 1821 m. (c) Typical appearance of type 2 FSV, cut into DMT. Faint type 1 and type 2 FSVs join the largest channel at high junction angles. CTX images P04_002560_2309_XI_50N329W and P04_002494_2310_XI_51N328W. Maximum elevation is −2462 m, minimum is −3428 m. (d) Type 2 FSV cut into dissected mantle terrain (DMT), but running beneath minimally dissected pasted-on terrain girdling hills. CTX tiles as Figure 3c. Maximum elevation is −3943 m, minimum is −4766 m. (e) Network of clustered FSVs. A trellis-like pattern of closely spaced type 1 FSVs runS down the steep inner wall of this crater. Junction angles are typically high. Channels lower down the network (higher Strahler numbers) are more likely to be wider (type 2). A prominent, slope-transverse type 2 FSV forms the downslope limit of the network. Type 2 FSVs appear to be floored by ridged DMT. CTX image P13_0059501401_XN_39S348W. Maximum elevation is 1965 m, minimum is 1165 m. (f) Imagery showing a network of FSVs overlaid on a 1 m resolution DTM derived from HiRISE, courtesy of E. Kite. Colorization of terrain has been exaggerated compared to Figures 3a–3e for clarity, and terrain slopes gently NW; maximum elevation is −4255 m, minimum is −4924 m. The central tributary upstream transitions smoothly from a type 1 to type 2 FSV in the downslope direction. The lower sections of the FSV below the confluence anastomose and have a notably lower sinuosity than the upslope tributaries. Inset graphs show elevation versus horizontal distance, both in meters, for sample extracted transects across the valleys. DTM built from HiRISE images ESP_016339_2295 and ESP_016260_2295.

Type 2. These are wider valleys, typically with distinct, nearly flat floors (e.g., Figures 3c–3e). Their cross sections are rectangular to slightly U shaped, with significantly higher valley aspect ratios (width/depth) than type 1 FSVs. Margins are parallel and flow paths have comparatively low sinuosity. They are typically less deeply incised into the surrounding terrain. Floors may show faint longitudinal lineations. Valley segments typically gradually shallow and narrow at their starts and ends, as the slope of the underlying terrain changes. In some cases, these valleys run under or emerge from beneath VFFs, DMT, or pasted-on terrain (e.g., Figures 3a, 3d, and 3e), but the vast majority do not.

Valley segments of both types are typically found in chains, where although the segments do not join, their orientation suggests that they were formerly connected (e.g., Figures 3b and 3e). Areas across which the valley is absent are normally local lows, giving the impression that the flow is "jumping" across depressions; this arrangement is most common on the lower gradient, hummocky terrains typical of the ejecta blankets outside the main craters in both localities. Chains of valley segments can be regionally extensive—the longest chain in the LVSW area is around 12 km, and the equivalent in Lyot is around 150 km (this valley in particular was noted by *Dickson et al.* [2009] as the most extensive young drainage on Mars). The median segment lengths are 0.40 km for LVSW and 1.18 km for Lyot (modes are 0.20 km and 0.70 km, and means are 0.73 and 2.05 km, respectively, due to positive skew toward longer valleys in both cases).

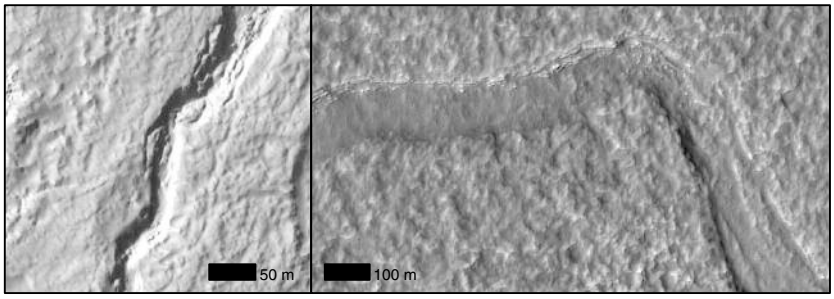

Figure 4. FSV textures at HiRISE scale. (a) Slope failures and landslides in a type 1 FSV. Image is centered at 11.630°E, 39.763°S. Image is ESP_016393_1400. (b) Typical morphology of type 2 FSV at HiRISE scale. In rare places, valley walls fragment, but most of the blocky texture on the north wall is intact layering emerging from the incised terrain. Floor texture is dominated by a valley-transverse ridged pattern, but occasionally (e.g., the southeast corner of the image) channel-parallel ridges and grooves can be seen. Image is centered at 30.712°E, 49.033°N. Image is ESP_016260_2295.

In areas where the density of FSVs is high, they can form drainage networks where the valleys integrate together in the regional downslope direction (e.g., Figure 3e). These networks may incorporate both types of FSV. Where so, type 1 valleys tend to be at the head of the network and type 2 farther downstream, where more valleys have merged (i.e., type 2 FSVs have higher Strahler orders). Type 1 valleys may form trellis patterns, draining off steeper terrain to join a single, lower gradient type 2 valley at high stream junction angles. This integration suggests that the two mapped types of FSV are in fact end-members in a continuum of form, as discussed further in sections 5 and 7.4.

Examination of the type 2 FSVs visible in the 1 m HiRISE DTM (Figure 3f) shows that these examples have floors between 3 and 7 m below the surrounding terrain, widths of 120 to 200 m, and aspect ratios of around 30 ± 10. Based on qualitative comparison of shadow lengths and bank widths, these values seem typical of type 2 FSVs around both study sites. Type 1 FSVs sometimes seem to be cut more deeply but probably seldom exceed a few tens of meters depth [cf. *Morgan et al*., 2009; *Mangold*, 2012].

Where FSVs of both types appear in HiRISE imagery, fine-scale modification of these landforms after formation is visible (Figure 4). In type 1 valleys, where sidewalls are steep, collapse and landsliding of the sidewalls of the valleys are common (Figure 4a). Valley floors that are not smooth (presumably not dust covered) are commonly textured with obvious landslide debris, or with hummocky textured material which is probably degraded landslide debris. Landsliding is rarer from the sidewalls of type 2 valleys, probably because they are less high (Figure 4b). Texture on the valley floors in these type 2 FSVs is revealed in HiRISE to be dominantly fine-scale rippling running across the valley, occasionally overprinting indistinct valley-subparallel undulations and ridges. The former is possibly an ice ablation texture, similar to that seen on other inferred ice bodies around the areas and reminiscent of those on linear debris aprons (LDAs) in eastern Hellas described as wind ablation features by *Pierce and Crown* [2003]. The latter is more enigmatic, perhaps related to ice flow in from the margins of the valleys after formation (analogous to lineated valley fill in the fretted terrain [*Carr*, 2001]), or perhaps representing degraded channel structures on the valley floors [*Howard and Moore*, 2011].

3.2. Landforms and Terrains Associated With FSVs

In some cases, FSVs are concatenated with two other much rarer landforms (Figure 5):

1. Ridges. In occasional cases, the downslope end (or, very much more rarely, the upslope end—see the southernmost valley in Figure 3f) of an FSV is followed by a ridge. The ridge appears to rise from the valley floor as the valley dies out. Both FSV types can abut ridges, and the ridge width mimics the FSV: Type 1 FSVs are associated with sharp-crested, narrow ridges and type 2 FSVs are associated with wider, flat-topped ridges which may show a ropey texture. In the most common examples, the ridge begins as the FSV ends; at other times there may be a gap between FSV and ridge. Most ridges exist in isolation from other ridges, though examples do exist of convergent, crosscutting, and divergent ridges, the last of these being most common. Very occasionally, a ridge can link two FSV segments; 105 ridge segments are mapped in LVSW, 28 in Lyot.
2. Mounds. Ridges sometimes transition to mounds at their downslope end. These landforms are flat topped and level with the crest of the upslope ridge but have steep, convex margins. They are typically broadly

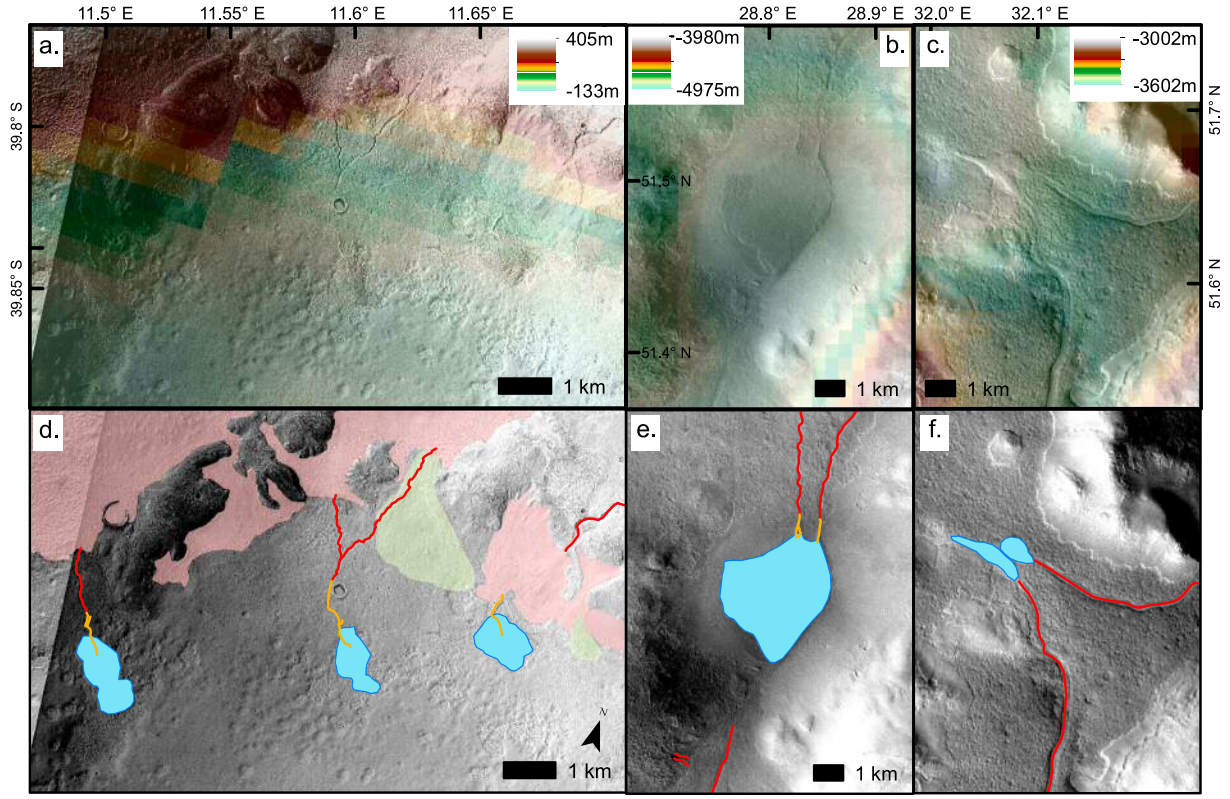

Figure 5. Rarer features associated with FSVs. (a–c) CTX images underlain by arbitrarily scaled DTMs to show local topography; (d–f) interpreted structures; red is FSV, orange is ridge, blue is mound. North is up. This figure is reproduced without coloration in the supporting information. FSVs draining the inner wall (sloping south) of a large crater in LVSW are shown in Figures 5a and 5d. Undifferentiated DMT and VFFs are shown shaded pink as they merge in this location. Green corresponds to enigmatic small fans, which we make no further attempt to interpret here other than to note the tiny channels crossing their surfaces are already apparently inverted but cut by the FSVs, and that thus they are older than the FSVs. Three FSV systems are visible; the central and western examples show complete concatenated downslope sequences of FSV-ridge-mound, as described in the text. In the easternmost example, there is a gap between the FSV and the ridge, probably because the system runs beneath the intervening VFF. Note the ridges penetrate a short way into the mounds. Note offset north. CTX images P15_006807_1391_XN_40S348W and P07_003827_1380_XN_42S348W. Two separate FSV-ridge segments connect to a single, structureless flat-topped mound, implying these systems were active concurrently, are shown in Figures 5b and 5e. The FSV-ridge transition coincides with the transition from dissected to undissected mantling terrain. The mound lies in a local, open hollow. A wider type 2 FSV is visible running on south (downslope) in the lower part of the image, and probably once connected with the upslope system. CTX image P21_009179_2308_XI_50N331W. Two smaller mounds at the end of type 2 FSVs are shown in Figures 5c and 5f. In these cases, no distinct ridge segments are present. CTX image P17_007821_2306_XN_50N327W.

teardrop shaped, narrowing up toward the connecting ridge, but with somewhat bulging and irregular outlines. Ridges may penetrate into the mounds, but the bulk of the mounds themselves are without obvious layering and do not have linear structures crossing them. The surfaces of the mounds are typically deeply but irregularly cracked and pitted, reminiscent of some of the textures described by *Mangold* [2003] on DMT as ice sublimation textures around existing fissures. Rarely, mounds can be connected directly to FSVs with no intervening ridge (e.g., Figure 5c). Isolated mounds that do not appear to be connected to ridges or FSVs are also recognized, but due to this are difficult to map unambiguously. The mounds are frequently positioned either immediately downslope of the snout of a VFF or its terminal transverse ridges (as described below), sometimes forming in lines along a present or inferred former VFF margin (e.g., Figure 2c). In other cases, a mound may form midway along the course of a chain of FSVs, implying that the mound postdates, or is synchronous with, at least a phase of FSV formation (e.g., Figure 5b). Sixty-two mounds have been mapped in the LVSW site, with a mean area of 0.37 km^2. Eighteen are recognized in the Lyot site, with a mean area of 2.98 km^2. Complete contiguous sequences of FSV-ridge-mound are rare, but still seen 15 times in total across both localities.

3.3. Bedrock

The stratigraphically lowest material in both areas largely appears with a surface texture which is rough and structureless on CTX scales (e.g., Figure 6a). At HiRISE scales, some low, randomly orientated, sharp-crested ridges are visible as part of this texture, and scattered boulders are visible on the surface, but it remains

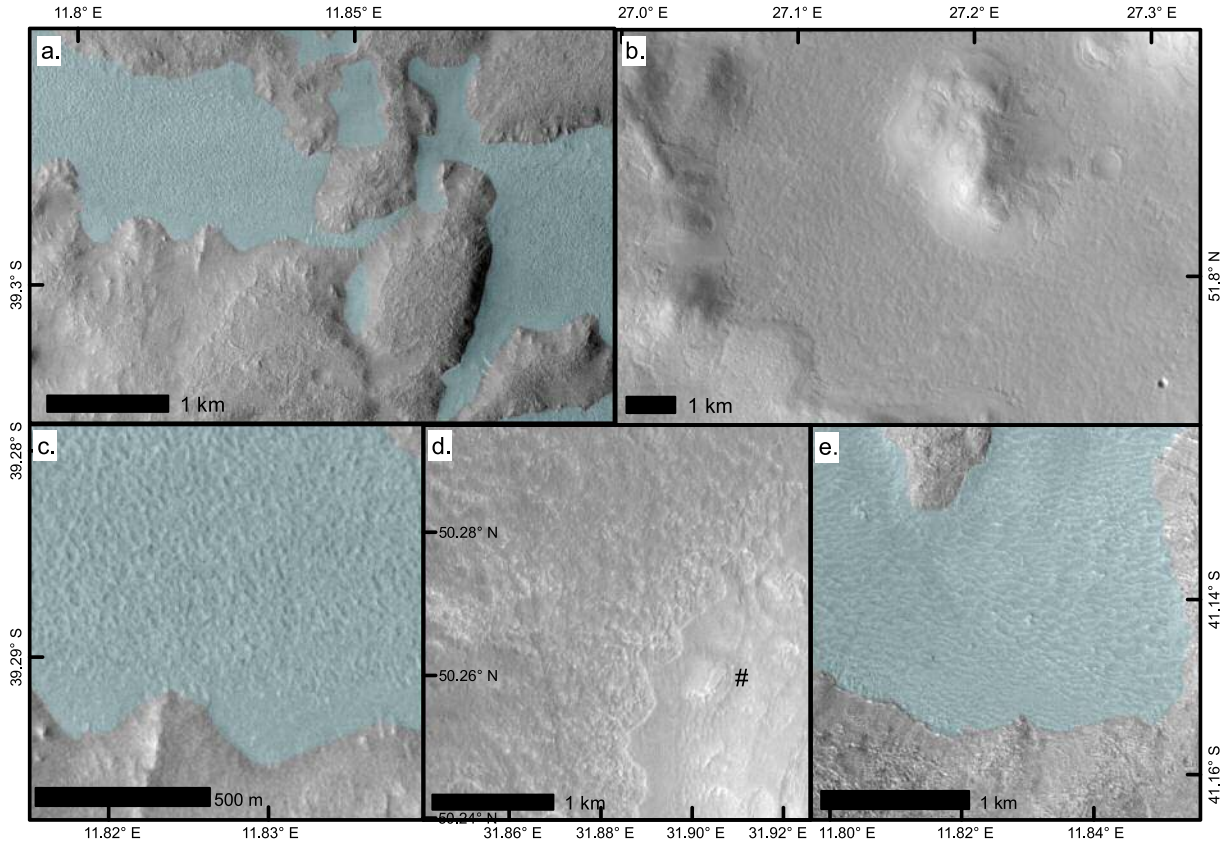

Figure 6. Different expressions of dissected mantle terrain (DMT) from around the study sites. North is up. This figure is reproduced without coloration in the supporting information. (a) Partially dissected, flat-lying terrain (blue) infilling topographic lows in LVSW. The hills are composed of "bedrock", as described in the text. Note that the stippled texture dies out toward the higher terrain. CTX image P07_003827_1380_XN_42S348W. (b) Partially dissected terrain in topographic lows in Lyot. Material is pasted on to steeper terrain in places and forms undissected benches around hills. The smoother surface mantling the central mound appears distinct from the downslope material beyond the scarp, but in other places nearby, scarps are only present occasionally, and the rough and smooth terrains seem to merge. This suggests they are the same unit, now modified by varying degrees of sublimation. CTX image P04_002626_2304_XI_50N332W. (c–e) Typical variation in pitting textures seen in DMT. Textures range from isotropic pitting to ripple-like ridges. Blue denotes DMT in topographic lows in Figures 6c and 6e, though where scarps are absent the margin is often hard to pick. In Figure 6d, the whole image is composed of DMT and dips slightly NW. Note that the bench (number sign) is well distinguished by a scarp on its west edge, but not on its north. Hints of multiple layers in the mantle are seen in the low mesa immediately west of the symbol. CTX images P07_003827_1380_XN_42S348W, P15_006819_2296_XN_49N328W and P17_007821_2306_XN_50N327W, and P07_003827_1380_XN_42S348W.

dominantly rough even at these higher resolutions. Small depressions amongst the rough texturing are commonly smooth floored. The material is commonly exposed in low hills or hummocks which poke through the mantling materials, as well as in local highs such as crater rims. These rough hills are commonly rounded at hillslope scales. We infer from the surface textures that this material has been heavily modified by dust infilling and impact gardening, and from the rounded hillslopes that diffusive mass wasting or mantling is important in its formation. In this study we term this material "bedrock," though it is possible that this unit is an icy regolith rather than true rock, especially if the hillslope rounding is due to a mantling process. Nonetheless, we infer from the overall topography of the sites that true bedrock (e.g., ejecta, central peaks, crater rim strata) is present shallowly beneath the surface.

3.4. Dissected Mantle Terrain, VFFs, and Other Possible Relict Ice Features

Dissected mantle terrain (DMT) [*Mustard et al.*, 2001; *Head et al.*, 2003] is characteristic of the majority of lower relief areas, and of local topographic lows, around both sites (Figure 6). Textures ranging from smooth to rough are apparent in this material at CTX scales, probably indicating variable degrees of degradation of these mantles. In Lyot, smooth, intact areas of mantle tend to hug the breaks in slope around the foot of uplands bedrock hills; farther from the hills, and separated from the smoother material by a low but distinct scarp, is rougher, more heavily dissected DMT (Figures 6b and 6d). In LVSW, the distribution of rougher and smoother DMT seems more random and less clearly demarked. In places, layering can be seen within these mantles (Figure 6d). At CTX scales, the texture of the rough terrain is quite variable, ranging from irregularly

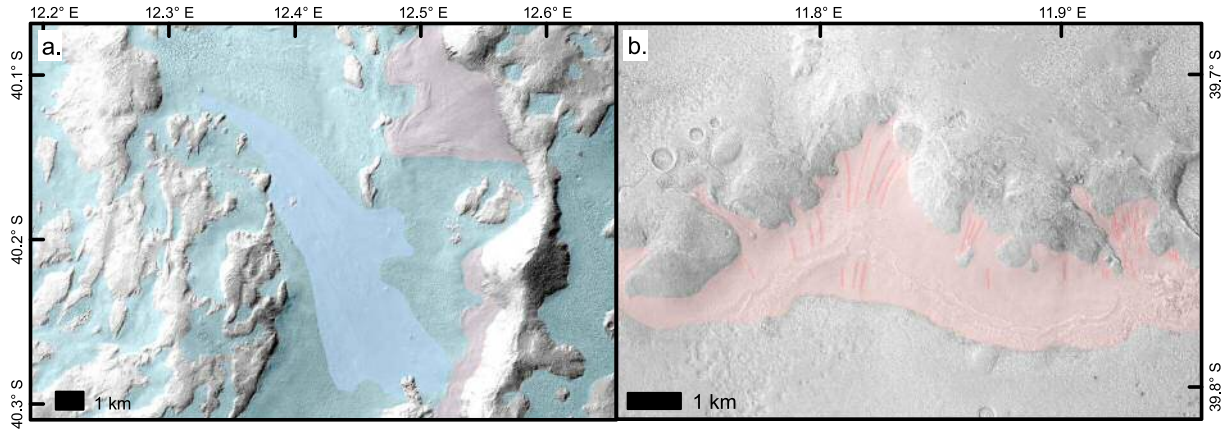

Figure 7. Examples of viscous flow features from study sites. North is up. This figure is reproduced without coloration in the supporting information. (a) A tongue-like longitudinally lineated VFF (darker blue), merging with the surrounding DMT (lighter blue), pooled in a topographic low between a crater ring to the east and hummocky hills to the west. A second set of transverse ridges adjacent to steep terrain, as in b, superpose this both the VFF and DMT (pink). CTX image P14_006596_1400_XI_40S347W. (b) Ridges (pink) girdling steeper terrain inside a crater (surface slopes south). Downslope lineae are visible through the finely ridged and pitted surface texture upslope of the terminal ridges. The material embays hollows on the break in slope from which it descends. This landform is interpreted as a degraded VFF/LDA. CTX image P07_003827_1380_XN_42S348W.

pitted surfaces to those showing wavy lineations reminiscent of ripples, to cracks at a variety of scales and geometries (see Figures 6c–6e). At HiRISE scales, a variety of open- and closed-cell vermiform brain terrain [*Levy et al*., 2009] and polygonal ground textures are seen, consistent with the interpretation that this material has high ice content. The DMT appears most often as low-relief surfaces in the bottom of topographic hollows and depressions. In some cases, it also forms the floors of stubby reentrants which branch away from these hollows. Following other authors [e.g., *Mustard et al*., 2001; *Head et al*., 2003; *Dickson et al*., 2009; *Fassett et al*., 2010], we interpret the DMT to be ice-rich mantling deposits, with the various surface textures seen corresponding to different degrees of degradation of the mantles by ice loss to sublimation [*Mangold*, 2003; *Pierce and Crown*, 2003; *Chuang and Crown*, 2005]. The fact that the DMT in both areas is somewhat cratered and hence not geologically recent also strongly suggests that it is insulated by a surface lag [*Williams et al*., 2008], and probably implies this material has a high dust or other rocky debris content that can form such an ablation lag as the surface degrades.

Other depositional landforms interpreted to be ice rich such as linear debris aprons (LDAs) and viscous flow features (VFFs) are also common in both sites and are distributed in a similar way in each locality. Here we define a VFF as a lobate or sheet-like structure showing either parallel or transverse surface lineations and associated with either compressional ridges or extensional troughs [e.g., *Milliken et al*., 2003]. We include LDAs within this definition [cf. *Head et al*., 2010], such that VFF describes all lobate structures or their degraded remnants around the areas, regardless of whether the body is prolate or oblate with respect to inferred flow direction in plan view. Two distinct forms are apparent. First, common in both sites are areas where the substrate shows VFF-like downslope lineations on a smooth surface, but transverse ridges are absent and the surface seems to merge with the surrounding DMT (e.g., Figure 7a). A second, more common form is seen where concentric ridges girdle steep terrain, equivalent to the "arcuate ridges" of *Arfstrom and Hartmann* [2005] and *Berman et al*. [2005]. Upslope from these features, faint downslope lineations may in some cases be visible beneath a dominant pitted or scalloped texture (Figure 7b), though often this lineation is not apparent. In some cases, these ridges superpose more extensive elongate structures (e.g., Figure 7a), sometimes crosscutting the underlying flow lineations, and hence are younger than them, as also noted by *Fassett et al*. [2010]. Following *Milliken et al*. [2003], *Arfstrom and Hartmann* [2005], and *Berman et al*. [2005], we interpret these features as recording the former presence of VFFs, which are now absent or very much reduced, presumably by volatile loss. A scarp is commonly developed on crater rims upslope of the ridges (e.g., Figure 7a), suggesting backwasting by erosion at the base of the slope.

Craters 2–8 km diameter in the study areas with well-preserved ejecta exhibit fluidized ejecta patterns, typically forming pancake craters [*Mouginis-Mark*, 1979]. Many craters are heavily altered, typically girdled internally by ridges like those found at the termini of VFFs, or by concentric crater fill [*Squyres and Carr*, 1986; *Levy et al*., 2009], and with rims that are rounded in cross section. As noted above, this rounding may imply either diffusive mass wasting or thick mantling is involved in modifying the crater forms [e.g., *Berman et al*., 2009].

4. Hypotheses for Formation of FSVs

Our qualitative observations indicate that the FSVs around our study areas share a number of distinctive properties: (a) found close to extant relict ice features; (b) association with enigmatic ridges and mounds; (c) preferential preservation on topographic highs; (d) flow paths that appear displaced from local topographic lows in some cases; (e) fresh appearance (implying "young," at least post-Noachian formation); and (f) found in chains, where individual segments have abrupt starts and ends. Prompted by such observations, we wish to use quantitative assessment of the geomorphology of these features to test possible formation process mechanisms and paleoenvironments for the FSVs.

We distinguish five possible formation mechanism hypotheses:

1. FSVs are cut by fluvial flow in open channels, in regionally extensive valley networks. The segmented and apparently topographically displaced flow paths seen now are consequences of post-incision deformation and preservational biases. This is the null hypothesis and is commonly implicitly assumed by previous authors who have worked on FSVs [e.g., *Berman et al*., 2009; *Dickson et al*., 2009; *Morgan and Head*, 2009; *Fassett et al*., 2010; *Howard and Moore*, 2011; *Jones et al*., 2011; *Mangold*, 2012].
2. Drainage was regionally integrated and open to the atmosphere, but with a succession of lakes forming in topographic lows, between channel segments. This might account for the preferential preservation of channels on local highs and not in local depressions. Headward sapping of channel overflow may be implicated in allowing channels to "burrow through" local highs.
3. The channels reflect flow in the subsurface and subsequent surface collapse to reveal the features. The counterintuitive drainage patterns seen in the imagery result from the channels following water table hydrostatic gradients, not topographic gradients.
4. Flow occurs in channels which very quickly freeze over, creating pressurized ice carapaces over the water courses [e.g., *Wallace and Sagan*, 1979; *Carr*, 1983]. This allows the flow to be displaced away from local topographic lows. This hypothesis does not necessarily rule out the presence of lakes within the drainage network.
5. Flow is occurring beneath a regional ice cover, with the weight of the overlying ice providing the hydrostatic head to drive channels in counterintuitive flow directions. Note that, again, lakes may be permitted to form along the chains of channels. This model does not demand thick (kilometer-scale; see section 7.3) ice, nor flow of the ice itself, just that the cover be regionally extensive. However, a cover of snow alone would probably be too permeable to allow the required pressurized flow to be sustained.

We can divide these hypotheses into two groups. Hypotheses 1 and 2 assume that when flow in the FSVs occurs, it does so exposed to the Martian atmosphere. Liquid water at the surface of Mars under present conditions is not stable. If exposed to the air, it will begin to simultaneously boil and freeze [e.g., *Conway et al*., 2011]. However, if the FSVs formed during a climatic optimum [*Dickson et al*., 2009], or were carved by brines [*Brass*, 1980], or indeed were cut quickly by unstable water before it froze and/or boiled, then flow in an eroded trough open to the atmosphere is likely. We note that gullies on Mars may form by this process [e.g., *Schon and Head*, 2011]. Hypotheses 3, 4, and 5 all require that the flow would be pressurized. Flow of water within enclosed conduits is a very plausible outcome on the surface of Mars. A number of authors have suggested that the tendency of water to freeze under modern Martian conditions may result in an armoring carapace of ice over any water courses [*Wallace and Sagan*, 1979; *Carr*, 1983; *Hecht*, 2002]. Such a shell of ice would have the advantage of increasing the partial pressure of water vapor in the enclosed space, thus stabilizing liquid water [e.g., *Hecht*, 2002; *Carr*, 2006]—though *Dickson et al*. [2009] emphasize that the atmospheric pressures at the bottom of Lyot would be high enough in the Late Amazonian to stabilize water without a cap. However, it would also result in the possibility of pressurized flow down the channel. It has also been suggested [*Clow*, 1987; *Costard et al*., 2002; *Christensen*, 2003; *Dickson et al*., 2009; *Fassett et al*., 2010; *Schon and Head*, 2011] that a viable source of water for young fluvial activity on Mars might be long-lived snowpack (firn) accumulations. These situations would also be conducive to the development of enclosed channels flowing beneath the snow. An end-member scenario for pipe flow would be flow beneath a thick enough snow accumulation that a glacier develops and would appear in our hypotheses within hypothesis 5. A number of authors have argued for locally extensive ice and glacier cover in the Martian midlatitudes at times in Martian history, including the Amazonian [*Kargel and Strom*, 1992; *Kargel et al*., 1995; *Head et al*., 2003], though due both to the lack of pervasive terrestrial-style glacial erosive features such as U-shaped valleys [*Head and Marchant*, 2003; *Marchant and Head*, 2007] and thermal constraints from modeling [*Kargel et al*., 2011;

Kargel and Furfaro, 2012], Martian Amazonian glaciers have often—though not exclusively [*Arfstrom and Hartmann*, 2005; *Banks et al*., 2008, 2009; *Hubbard et al*., 2011]—been inferred to be cold based and frozen to their beds, without the ability to sustain liquid water at this interface.

This distinction provides a key, quantitative test of our null hypothesis—is the distribution and quantitative geomorphology of the FSVs consistent with Earth-like flows in open channels, or are there signs that the flow was pressurized? Here we briefly outline the distinctions that we will use to discriminate between them.

Open flow. This situation is essentially analogous to a terrestrial river. The ability of the flow to erode its bed or transport sediment is thought to be determined primarily by the shear stress it exerts on its bed and banks, which is in turn a function of the discharge through the channel and the surface slope of the flow. This surface slope approximates the slope of the channel bed at the channel scale and upward [*Howard and Kerby*, 1983; *Howard*, 1994; *Hancock et al*., 1998; *Whipple and Tucker*, 1999]. Likewise, the weight of the water itself is responsible for its flow downhill; shallow water flows down the steepest topographic gradients in the landscape.

Pipe flow. In a full pipe water exists under pressure. Pressure is maintained by the walls of the pipe and by the hydrostatic pressure of water elsewhere in the pipe. Discharge, Q, along such a conduit is propelled not by the weight of the water itself, but by gradients in this pressure field; it can be described by

$$Q^2 = \frac{16r^5}{\rho f_D}\frac{\mathrm{d}P}{\mathrm{d}x} \tag{1}$$

where ρ is the density of the fluid, r the radius of the pipe, f_D the Darcy friction factor, and $\mathrm{d}P/\mathrm{d}x$ the change in pressure along the pipe, assuming water is conserved in the pipe (the Darcy-Weisbach equation). In the case where water is piped beneath an overburden such as a mass of ice, this pressure gradient is to first order governed by the slope of the ice surface, S_{ice} [*Röthlisberger*, 1972; *Shreve*, 1972]. By isostatic balance of pressure in the ice overburden, and assuming efficient compaction of snow into ice, this gradient can be shown to be around 11 times more important than the bed gradient in determining pressure gradients within the ice and hence ice flow directions and movement of water within and below the ice [*Shreve*, 1972]. Dominance of the ice surface slope over local topographic slope can lead to basal water flow up local topographic slopes and to displacement of flow paths away from local topographic valley bottoms [e.g., *Sugden and John*, 1976].

This analysis indicates the key distinctions between these two scenarios. Shallow open flow in steep terrain should always follow topographic gradients. It flows in the lowest parts of a landscape (i.e., valley bottoms), travels downhill, and follows the steepest possible lines of descent. In contrast, because it is governed by the overlying ice burden not its own weight, pipe flow beneath ice can both flow "uphill" against local topographic slopes, and likewise in some cases can head in directions which do not correspond to local topographic steepest downslope paths. On Earth, these properties form a key part of the toolkit of researchers looking to identify subglacial channels [e.g., *Sugden and John*, 1976; *Shreve*, 1985].

5. Analysis Methodology

These key distinctions form the basis for our analysis. We use mapping of the FSVs (see section 3), extraction of their widths and local slopes, and analysis of the topographic drainage structures of the regions to discriminate between these two possibilities and then between the various formal hypotheses possible within each of them. Note that we map and present data describing the two types of FSV separately, but will show in our analysis that our results are entirely consistent with the two types being end-members in a continuum of form, probably controlled by the discharge that cuts the FSV (section 7.4). Thus, we perform analysis treating all the FSVs as a single data set.

5.1. Valley Width and Local Slope

We measured the associated rim-to-rim valley widths of the FSVs, taking one width measurement approximately every 100 m of valley length, and requiring at least three width measurements per valley. These measurements yielded mean widths for each valley segment. We have measured rim-to-rim valley widths instead of valley floor widths since where FSVs are narrow, the floors may be impossible to define in CTX (i.e., type 1 FSVs; see section 3.1) and we want a way of comparing the widths of the two valley types. We note however that there appears to be little systematic variation of incision depth into the landscape with FSV width. Thus, we can assume that valley rim width acts as an acceptable proxy for valley floor width in

most cases, though acknowledging the potential biases from sidewall slopes and incision depths. It remains unclear whether the valley floors correspond to channel widths.

Values of local topographic slope were derived for each DTM using the standard algorithm in ArcGIS: A plane is fitted across each 3×3 window in the DTM, and the slope of the plane determined by the average maximum technique [*Burrough and McDonell*, 1998]. The slope values of cells in which FSVs are found were then extracted. Although these slopes are not the true bed slopes of the FSVs, which sometimes diverge from regional downslope directions, this method remains appropriate as we wish to characterize the surface steepness of cells where FSVs are seen, rather than the slopes of the FSVs themselves (see section 6.2).

5.3. Drainage Pattern

Ideally, we also wish to examine the distribution of the FSVs with respect to drainage patterns (watersheds and flow paths) derived from the shape of the topographic surface, but this is considerably more problematic than analysis of local slope. The integration of synthetically derived drainage patterns across a DTM landscape can be fundamentally altered by small amounts of noise on the surface [*Tribe*, 1992]. This problem is amplified in low-relief landscapes and those which have not been extensively shaped by fluvial processes, both of which are true in our Martian study sites [e.g., *Mest et al*., 2010]. Traditional terrestrial solutions such as "fill" functions in GIS software or "snapping" of FSVs onto the extracted drainage structure are not appropriate for this context; we wish to investigate whether the FSVs reflect the topographically defined drainage structure, and these analyses implicitly assume that they do.

Instead, we examine the drainage pattern of the DTMs at a variety of arbitrary resolutions, from the highest resolutions available for HRSC (75 m or 250 m) through resampling of the DTMs at 300, 463, 1000, and 2500 m. This resampling has the effect of removing progressively higher amplitude and larger wavelength roughness from the landscape without assuming hydrologic connectivity. This progressive generalization allows integration of drainage over progressively larger areas of the landscape and increases the average size of each internally drained basin. We can assess the relation of the FSVs to their source areas in a more unbiased way by looking at their distribution under the full range of these DTM resolutions. This resampling to progressively lower resolutions also crudely mimics the effect of increasing ice cover over the landscape. Increasing ice cover will blanket the local topography and smooth out fine topographic detail in the surface of the ice; thus by resampling our DTMs to coarser resolutions and extracting the drainage networks, we are also mimicking the surface slopes of the putative ice cover and thus revealing some sense of the large-scale drainage structure under the ice. It is not clear where the boundary between removal of noise and removal of fine scale (real) topography actually lies, in part because varying thicknesses in a real ice cover around the landscape would lead to different amounts of smoothing in different places. This prevents a true quantitative hypothesis test. We can however use our different resolution resampled DTMs as a semiquantitative test for the effects of ice cover. If the FSV pattern mimics the drainage pattern extracted for qualitatively "large" amounts of smoothing ($\sim >1$ km resolution pixels) but not at higher resolutions, this provides support for the ice cover scenario. If the drainage follows the extracted patterns at intermediate to high resolutions, we do not have support for the ice-covered hypothesis. The strongest test will be provided by the valley patterns nearest to the highest amplitude basin margins, i.e., the ones retained in the coarsest resolution resampling, which are almost certainly not noise in the DTMs.

5.4. Buffered Crater Counts

We also wish to constrain the ages of the FSVs in these areas, since this will help us constrain possible formation mechanisms later in this paper. We date the FSVs in each locality using a buffered crater count method [*Tanaka*, 1982; *Wichman and Schultz*, 1989; *Namiki and Solomon*, 1994; *Fassett and Head*, 2008; *Howard and Moore*, 2011]. This method aggregates superposed craters on all FSVs in each study site and thus assumes a single episode of FSV formation in each case. Qualitatively similar degradation of the FSVs in each locality suggests this assumption is reasonable. Inspection reveals that the few craters close to the FSVs are small (<1 km diameter, D) and lacking in well-defined ejecta deposits. This makes it extremely challenging to tell whether a crater postdates FSV formation unless the cavity actually intersects the valley. Thus, we adopt a very narrow buffer, counting only those craters which intersect the FSVs. We count all craters $0.2\ \text{km} < D < 1\ \text{km}$ (no intersecting craters are $D > 1$ km), and calculate potential target areas using size-dependent bins extending out from the margins of each FSV. The 200 m cutoff is chosen to ensure that all counted craters are the same

scale or larger as the widths of the FSVs they intersect. This ensures that we are not missing impacts that have been hidden by mantling. A fuller description of this method can be found in the supporting information.

The small numbers of craters seen in the buffers (<10 in both cases) immediately tell us that the features are qualitatively "young," but also mean that conventional dating methods using crater count plots [e.g., *Hartmann*, 2005] are not appropriate to this setting. Instead, we use a Poisson distribution probability model to constrain likely ages for the structures. We calculate the expected number of impacts per bin following the crater size-frequency distributions of both *Ivanov* [2001] and *Hartmann* [2005], following *Werner and Tanaka* [2011], for comparison with the observed number of impacts. As only a small total number of impacts are observed, we assume a Poisson distribution that adequately approximates the probability of intersection of a crater and an FSV. This allows us to determine the 95% confidence intervals on the expected number of impacts, N_I, using statistical tables, where

$$Pr(N_I \leq n) = \sum_{\lambda=0}^{n} e^{n} \frac{n^{\lambda}}{\lambda!} \tag{2}$$

These can be inverted using the Ivanov and Hartmann distribution models to give statistically robust age brackets for the FSV networks in each locality (see supporting information). It is possible that ice mantling of these features will affect the absolute ages we derive for these localities; we discuss this possibility further in section 6.4.

A diagram describing the crater counting technique along with a fuller description of the method can be found in the supporting information.

6. Analysis Results

6.1. Distribution of FSVs

We have systematically mapped 761 distinct FSV segments across 66,000 km^2 of CTX imagery in the LVSW area and 881 distinct segments across 99,000 km^2 of imagery in the Lyot area (Figure 2). The corresponding valley length densities are 0.007 km^{-1} (LVSW) and 0.018 km^{-1} (Lyot). The valleys are unevenly distributed across both landscapes, however. In LVSW, they are most strongly concentrated inside and outside the rim of an 80 km terraced Late Hesperian [*Fassett et al.*, 2010] crater (number sign) to the west of center of the mapped area. Significant concentrations also exist inside the most proximal walls of neighboring rimless, older craters, and also in a second 70 km crater of similar morphology 130 km away to the south-southeast (dollar sign). Lower densities also appear around craters and occasionally on intercrater plains to the far east of the mapped area. Valleys are uniformly absent on smooth, low-gradient terrain, wherever it is found, and conversely appear more common on steeper, rougher, or more hilly terrain. In the Lyot area, FSVs are found throughout the interior of the crater and also in its ejecta. Valleys are not found on smooth, flat terrain, which means they are found more rarely far from the crater rim, as the textured and hilly ground associated with its ejecta and interior dies away to be replaced by flat intercrater plains. Inside Lyot, the FSVs appear to be better integrated than in the LVSW area, with frequent confluences joining on average longer valleys. A set of FSVs of similar width and orientation runs concentrically around the inner ring of the crater between around 90° and 200° (from i to ii in Figure 2b), toward which numerous other FSVs drain; following *Dickson et al.* [2009], we interpret these FSVs to together form a single flow path.

In LVSW, 67% of valleys are type 1 and 33% type 2. In Lyot, the situation is reversed, with 36% type 1 and 64% type 2. In neither case is there any apparent spatial pattern at the whole-map scale in the distribution of the two valley types around the landscapes.

Very rarely, FSVs are contiguous with or very close to the VFFs or ridges we infer were deposited by former VFFs [cf. *Fassett et al.*, 2010]. In such cases, valleys are found either immediately outside or inside the ridged and corrugated margins of these features, orientated parallel to inferred VFF flow direction (i.e., regionally downslope), in many cases appearing to start at the feature margin. We emphasize however that for the vast majority of FSVs, there is no extant VFF at the head of the segment chain.

Lyot crater dates to the Early Amazonian [*Greeley and Guest*, 1987], and the widespread stippled material into which many of the FSVs are cut dates to the Middle Amazonian [*Dickson et al.*, 2009], while the 80 km diameter crater which has the highest concentration of FSVs in the LVSW area was dated by Fassett and colleagues to

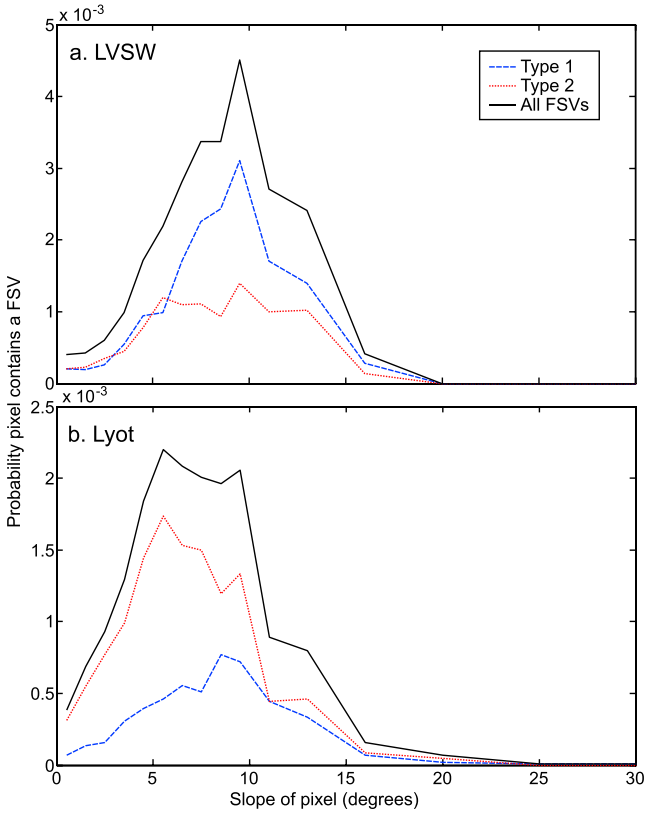

Figure 8. Dependence of FSV spatial distribution on local surface slope for both (a) LVSW and (b) Lyot study areas. Solid lines represent distribution considering all FSVs together; the dashed (blue) and dotted (red) lines break this down for the type 1 and type 2 subpopulations respectively. Local slopes are derived using HRSC DTMs resampled to 300 m/pixel in both cases. Similar graphs were also examined for other spatial scales (250, 463, 1000 m/pixel) using both HRSC and MOLA DTMs for both field sites, but did not differ significantly from the distributions shown.

around the Late Hesperian [*Fassett et al.*, 2010]. These dates provide maximum ages constraints for the FSVs in each case and demonstrate that they are a distinct valley population from the widespread valley networks [*Howard et al.*, 2005; *Fassett and Head*, 2008] and outflow channels [*Baker et al.*, 1992; *Tanaka et al.*, 2005] formed much earlier in Martian history.

6.2. Local Slope and FSV Width

The distribution of FSVs around the landscape is strongly dependent on local surface slope (Figure 8). We derive a probability that a given pixel contains an FSV at a given slope by normalizing the distribution describing the number of pixels at each slope containing FSVs by the distribution of local slope across the landscape as a whole. In both study areas, the probability a given pixel contains an FSV rises from near zero where slope is zero to a maximum, and then falls to zero again by a slope of around 20–25°. Type 1 FSVs show a well-defined peak in abundance in pixels with slopes of 9–10° in both study sites. Type 2 FSVs show a much flatter distribution between 5° and 13° in LVSW and in Lyot a well-defined peak in abundance at 5–6°. Because the type 1 FSVs are dominant in LVSW and type 2 in Lyot (see section 6.1), the resulting distributions considering all FSVs show peaks at 9–10° for LVSW and 5–6° for Lyot. These results are robust across a range of resolutions for the DTMs (250–1000 m) and across both the HRSC and MOLA data sets.

The average widths of FSVs vary both between locality and between type of FSV. In LVSW, the overall mean valley width is 33 m (20 m standard deviation); the mean width of type 1 FSVs is 26 m (standard deviation (s.d.) 10 m), and the mean width of type 2 FSVs is 46 m (s.d. 26 m). In Lyot, the overall mean valley width is 75 m (s.d. 56 m); the mean for type 1 is 46 m (s.d. 16 m), and the mean for type 2 is 91 m (s.d. 64 m). The expected offset between type 1 and type 2 valleys is apparent, based on their respective definitions, but presuming that these are end-members representing a continuum of discharges and noting the overlap in the standard deviations, we treat the data set as a whole.

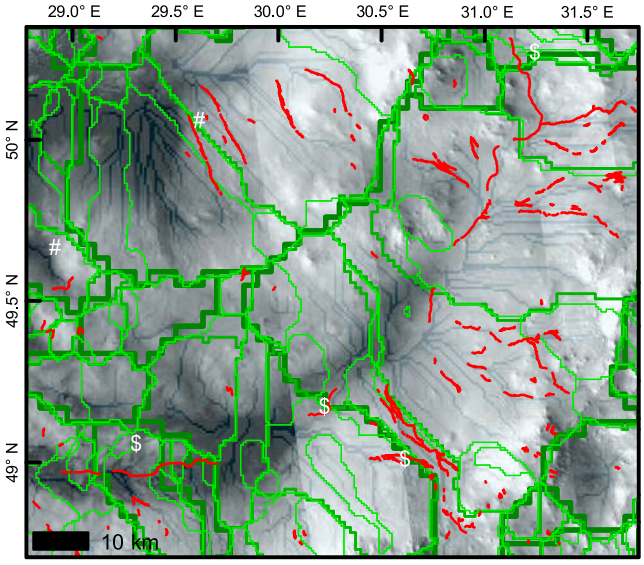

Figure 9. Interaction of mapped FSVs (red) with DTM-derived possible drainage structures, for a representative field of view in Lyot crater. North is up. Green lines show extracted basin margins for 463 m/pixel (light, thin), 1 km/pixel (mid-green, intermediate thickness), and 2.5 km/pixel (dark, thick) DTM resolutions, using MOLA data (HRSC data shows equivalent patterns). The associated flow accumulation pathways for the 463 m/pixel resolution DTM are shown in blue beneath the CTX base image. In most instances, the mapped FSVs tend to follow the extracted flow paths, though in a nontrivial number of cases they crosscut them (e.g., number sign). Note that FSVs frequently crosscut the extracted basin boundaries. This behavior is common for the 463 m/pixel basins, but still occurs even for the coarsest, 2.5 km/pixel, resolutions (e.g., dollar sign).

6.3. Drainage Pattern, Divide Breaching, and Uphill Flow

Comparing FSV distribution to the drainage patterns (watersheds and flow paths) derived at each DTM spatial scale, it is immediately apparent that although the orientations of FSVs broadly follow the flow paths derived from in the DTMs, in large numbers of cases, FSVs do not follow these paths (Figure 9). At small pixel sizes and in both study sites, large numbers of valley segments cross from one enclosed basin to another (Figure 10). At such resolutions, it is possible some of this behavior is driven by noise in the DTMs as opposed to representing valleys moving between "real" internally drained basins, as described in section 5.3. However, our resampling procedure (section 5.3) reassures us that examples do still occur at all pixel resolutions, including up to 2.5 km smoothing (e.g., Figure 9); the resampling removes many of the more subtle convexities present in the landscape, but ensures that those that remain are examples of FSVs breaching regionally significant drainage divides. Tables 1 lists the relative abundances of FSVs intersecting the boundaries of DTM-derived drainage basins at each available resolution and for both HRSC and MOLA data.

As expected, examining the individual long profiles of almost all valleys which appear to cross drainage divides reveals some convexity (e.g., Figure 11). At higher resolutions, many of the valleys breach low-amplitude drainage divides. These are the examples which disappear during resampling of the DTMs to coarser pixel sizes, as seen in the decrease in abundance with decreasing DTM resolution (Table 1). For these low-amplitude convexities, it is not clear to what degree the apparent breaching of the divides might be due to error in the DTMs, slight mislocation of the FSVs, or narrow, deep gorging of the FSVs into the drainage divide. However, we can be considerably more confident that the FSVs that breach drainage divides even in the lowest-resolution DTMs are real examples of uphill flow. In these cases, the convexities which define basin boundaries must be considerably higher and wider to have survived the resampling procedure, and are very unlikely to result from noise or systematic error in the DTM.

We confirm this by examining the individual long profiles of a subset of these valleys that (a) extend significant distances away from the divide on both sides, (b) are well defined, and (c) are wide, to increase penetration of the HRSC DTM into the valley. Figure 11 shows typical examples of these valleys and their long profiles. We present both HRSC and MOLA data to demonstrate the existence of the convexities in both independent data sets. In many cases, valleys rise around 20 m against the topographic gradient in order to pierce the drainage divides; in the longest valley in Lyot, the amplitude of the undulations can exceed 200 m. For the widest valleys ($>$150 m) in Lyot, where we have access to 75 m/pixel HRSC DTMs, we can be confident that these long profiles are directly sampling the floors of these FSVs; in the majority of other cases, likewise shadow length implies that the FSVs cannot be deep enough ($>$20 m) to allow the channel to cut the divide without also having to flow uphill. In addition, in a significant number of cases, the channel width appears to increase markedly, typically $>$30%, as the FSV crests the drainage divide and begins to again flow with the topographic gradient (Figure 10). In some instances, this is associated with a slight change in meander wavelength at the convexity. For the longer FSVs, where a number of individual segments form a chain (e.g., Figures 3a, 3b, and 11), a number of these segments also climb around 10 m against the local gradient, even where a drainage divide is not present in the 2500 m/pixel drainage extraction. These ascending valley segments

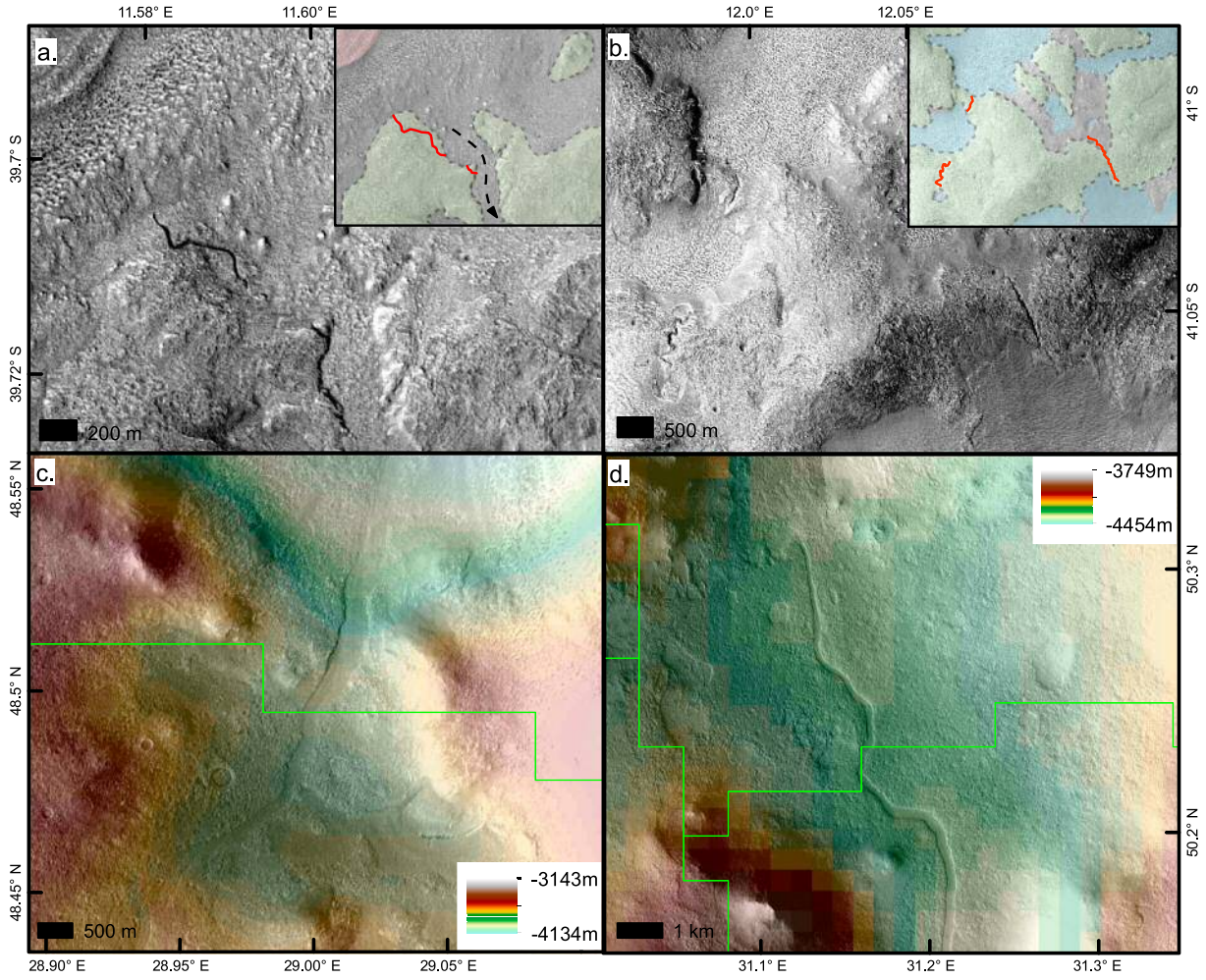

Figure 10. Qualitative evidence for uphill flow in FSVs. North is up. This figure is reproduced without coloration in the supporting information. Examples of counterintuitive flow directions in FSVs at sub-DTM scales. (a) FSV flowing along sidewall of a small valley, then cutting through a spur. CTX image P07_003827_1380_XN_42S348W. (b) Type 1 FSVs breaching drainage divides between local depressions. CTX image as Figure 10a. (c, d) Abrupt change in type 2 width as FSVs cross drainage divides. Underlying DTM scales are exaggerated for clarity; extracted 1 km/pixel basin margins are shown in green as in Figure 9. CTX images P21_009179_2308_XI_50N331W and P20_008744_2305_XN_50N331W, and P04_002560_2309_XI_50N329W and P04_002494_2310_XI_51N328W.

also correspond to areas where the qualitative shadow distribution across the CTX imagery suggests that the valleys are flowing uphill, further reducing the likelihood that these are false positives. This observation suggests many of the FSVs breaching low-amplitude drainage divides probably also represent real instances of flow uphill, though the maximum resolution of our DTMs prevents a robust assessment.

Table 1. Numbers of FSVs Breaching Drainage Divides at Varying DTM Resolutions

	LVSW			Lyot		
DTM Type and Pixel Resolution (m)	Mean Basin Area (km^2)	No. of FSVs	Percentage of FSVs	Mean Basin Area (km^2)	No. of FSVs	Percentage of FSVs
HRSC	-	732[a]	-	-	639[a]	-
HRSC 300	28.2	66	9.0	7.7	260	40.7
HRSC 463	34.5	72	9.8	13.6	225	35.2
HRSC 1000	65.3	50	6.8	51.9	102	16.0
HRSC 2500	227.9	20	2.7	284.7	55	8.6
MOLA	-	762[a]	-	-	881[a]	-
MOLA 463	34.1	74	9.7	26.8	146	16.6
MOLA 1000	107.8	40	5.2	72.2	104	11.8
MOLA 2500	420.3	15	2.0	295.9	57	6.5

[a]Refers to total number of FSVs contained within area of DTM.

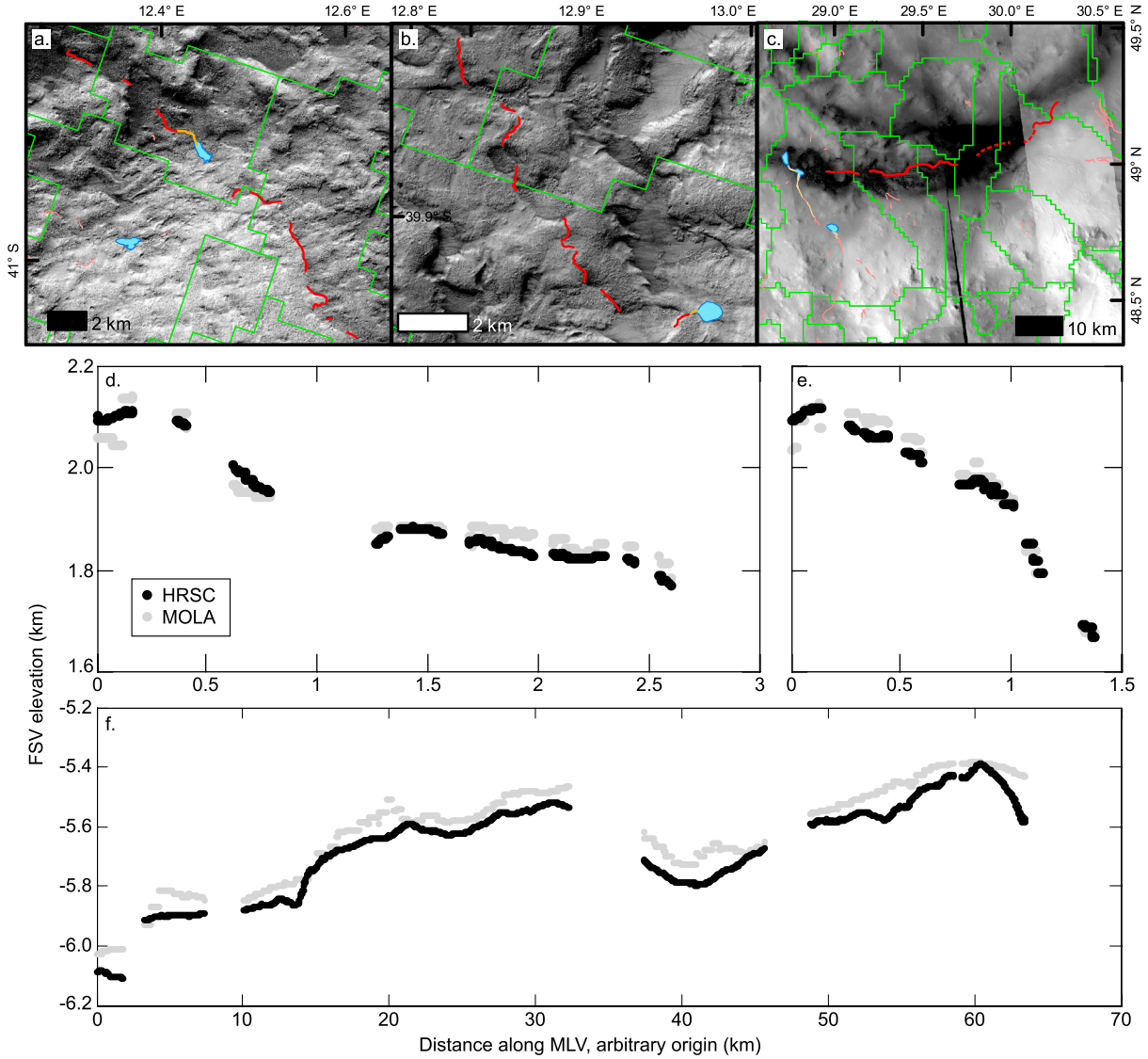

Figure 11. Quantitative evidence for undulose FSV long profiles. (a–c) Examples of long chain FSV systems from both LVSW and Lyot, which are seen to cross extracted drainage basin boundaries at all scales (basin margins at 1 km/pixel are shown in green). Chains shown in Figures 11d–11f are shown bold red, other FSVs are shown in thinner pink. In Lyot, this FSV chain is part of the axial drainage system in the crater inner ring; the dashed sections correspond to areas where the position of the FSV is clear, but its width is not. Green lines represent extracted drainage basin boundaries at 1 km/pixel, as shown in previous figures. CTX images P14_006596_1400_XI_40S347W; P13_006240_1419_XN_38S347W; and P21_009179_2308_XI_50N331W, P20_008744_2305_XN_50N331W, P15_006740_2287_XN_48N330W, P20_008678_2292_XN_49N330W, P03_002415_2310_XI_51N330W, and P04_002560_2309_XI_50N329W. (d–f) Extracted raw DTM elevation data for corresponding FSV chains shown in Figures 11a–11c. Vertical exaggeration is 2 times. Gray points are from MOLA data at 463 m/pixel; black points are from the highest resolution HRSC data available (250 m/pixel in LVSW, 75 m/pixel in Lyot). No smoothing has been applied to the data in either case. Note that the two data sets are in close agreement and reveal very similar profile shapes, though the MOLA data are considerably noisier, as expected. The convexities seen in the profiles correspond to apparent uphill sections seen in the imagery.

6.4. FSV Ages

Our buffered counts on craters $D > 200$ m reveal three craters in LVSW and six craters in Lyot which intersect and unambiguously postdate FSV formation. Assuming a Poisson distribution, the 95% confidence intervals on the expected number of impacts for the two areas from these numbers of observed craters are 1.1 to 7.2 (LVSW) and 2.9 to 11.6 (Lyot). Assuming the *Ivanov* [2001] and *Hartmann* [2005] crater size-frequency distributions, these expected numbers of crater impacts are inverted to give ages. Because the two crater distributions make comparable predictions at small crater sizes [e.g., *Werner and Tanaka*, 2011], the solutions we calculate under each model are in fact very similar. For LVSW, the most likely age for the FSVs is 135 Ma; the youngest and oldest possible ages are 50 Ma and 324 Ma, respectively (95% confidence). For Lyot, the most likely age for the FSVs is 60 Ma; the youngest and oldest possible ages are 29 Ma and 116 Ma, respectively. The

larger error for LVSW is due to the smaller potential target area created both by the smaller total mapping area and the lower FSV density in this locality. The confidence interval for the LVSW FSVs is entirely contained within the Late Amazonian under the Ivanov model, but could plausibly also date to the end of the Middle Amazonian (>235 Ma) under the Hartmann model [*Werner and Tanaka*, 2011]. The Lyot FSVs definitely formed within the Late Amazonian regardless of which age model is selected. Note that the ages derived for each area are statistically identical.

This paper's thesis is that these FSVs probably formed beneath an ice cover of order 10^1–10^2 m thick. If such a cover were sustained for a significant duration after the formation of the FSVs, this would have the potential to significantly alter our absolute formation dates: The Late Amazonian age we derive would be the deglaciation age, not the valley formation age. We will go on to argue on the basis of the positions of the mounds associated with the FSVs that the cutting of the valleys is genetically linked to the wasting of the ice cover, and in this situation, the ages we derive remain accurate. However, at the least the indistinguishable crater densities we obtain tell us that these two landscapes have shared a common history and have been armored by ice with similar effectiveness. The lack of large craters which would be capable of breaking through an ice shell (>500 m diameter, assuming a width/depth ratio of 5 and 100 m of ice) also provides a harder though wider age limit for these FSVs: Under a Poisson distribution, if we observe zero craters >500 m diameter across both sites, an expectation of three craters is the maximum possible at 95% confidence, equating to maximum surface ages of 800 Ma (Hartmann) or 940 Ma (Ivanov).

7. Discussion

7.1. Flow Uphill of FSVs

Our analysis of the HRSC DTMs (Table 1) shows robustly that at least tens of FSVs around both study sites are associated with local increases in valley floor elevation of ≫10 m in the downstream direction (as defined by regional slopes). With a lower degree of confidence, corresponding to smaller increases in bed elevation, this number may exceed 100 FSVs. For this to be the case, we must accept one of the following scenarios:

1. The FSVs were deposited in a conventional flow-downslope network. Subsequently the land surface has been warped by nonuniform deformation in the shallow subsurface. Possible mechanisms include differential compaction in current topographic lows compared to the adjacent highs, or melting/sublimation of ground ice in the shallow subsurface beneath the FSVs. We note that mechanisms of erosion or deposition of the actual surface cannot work, as the FSVs themselves are still visible, having not been buried or eroded away. Deep subsurface mechanisms are also not viable given the short (kilometer) wavelengths of the implied deformation. There is also no evidence for shallower, thin-skinned type tectonics (fault scarps, offset layers, folded layers) that could potentially produce deformations at these wavelengths.
2. The observed slopes are representative of the slopes at which the FSVs formed. If this scenario is true, we must reject hypotheses 1 and 2 from section 4 and accept that the flows which carved the FSVs were pressurized, and that a cap—of ice or rock—was present over the channels at the time of formation.

These hypotheses are testable with our data. Post-incision deformation of the surface by differential volume changes in the subsurface (scenario A) is possible, but unlikely. The form of the FSVs themselves suggests that the topography at the time of their formation corresponds to the current topography. Where FSVs form chains out on the intercrater plains, they commonly head toward neighboring basins, suggesting these basins were present at time of formation (e.g., Figures 10b and 11b). In a chain, FSVs are noticeably more likely to be absent in a depression than on a ridge (e.g., Figures 3, 10, and 11). Perhaps most tellingly, the planform of larger individual FSV segments can sometimes be seen to change as they pass over a drainage divide, with the return to downslope flow associated with a rapid increase in channel width (e.g., Figures 10c and 10d). For this to occur, the change in slope corresponding to the hill crest must have already been present when the FSV was formed.

We thus favor scenario B—the formation of the FSVs under pressurized flow beneath a now-absent cap—and one of hypotheses 3 (subsurface flow), 4 (ice carapaces), or 5 (regionally extensive ice cover) must be true. We can also discriminate between these possibilities with the data and observations we have already presented. Formation in the subsurface is very unlikely. Not only does it demand some form of collapse of the surface to reveal the valley, for which there is no other evidence (e.g., collapse pits elsewhere in the landscape, rubble in the bottoms of the FSVs), but also many of the FSVs meander, often quite tightly. Subsurface flow would have

to be occurring slowly through a permeable substrate (i.e., Darcy flow [see, e.g., *Barnhart et al*., 2010; *Levy and Fountain*, 2012]). Such velocities (probably limited to $\ll$1 mm/s, even in extremely permeable, 10^{-9} m^2, soil) mean that significant superelevation and oscillatory flow could never develop at putative subsurface meander bends [*Leopold et al*., 1960; *Howard and Knutson*, 1984]. Back-of-the-envelope calculations following Leopold et al. suggest superelevation would be of maximum order micrometers for channel geometries characteristic of our FSVs. Without superelevation, the helical flows characteristic of meandering flow cannot develop. In addition, without the ability to freely physically transport sediment grains in the subsurface, the feedbacks between sediment transport and deposition, and channel flow field thought necessary to sustain meandering cannot develop [see discussion in *Knighton*, 1998, chapter 5]. To our knowledge, tightly sinuous flow paths have never been observed as a consequence of subsurface flow on Earth. We postulate that subsurface flow and flow path sinuosity are fundamentally incompatible.

Flow beneath ice carapaces locally developed over each FSV cannot be conclusively ruled out but is unlikely. The pressures likely to develop in a typical pressurized FSV can be estimated to order of magnitude by calculating the pressure developed by the static head as the channel climbs ~20 m vertically uphill; this is likely to be around 10^5 Pa. The pressure associated with the most extreme uphill climb in either area (~200 m, in the ring valley of Lyot) would be around 1 order of magnitude greater. These values do not exceed approximate tensile strengths of an ice cover (~10^6 Pa [e.g., *Currier and Schulson*, 1982; *Lange and Ahrens*, 1983]), indicating a thin cover is mechanically plausible. However, the fact that some FSVs in this study do flow upslope makes this physically implausible. Flow against local gradient implies that the cap on the flow must have already been in place before discharge up the slope occurred. A conventional carapace model for flow calls for the carapace to form after the flow has begun, by surface freezing of the discharge itself; this cannot be the case for flow uphill under a thin cover. Having the cover in place before flow occurs demands a regional-scale ice blanket and thicknesses greater over the depressions than over the highs. This conclusion is reinforced by the regional distribution of the FSVs themselves (Figure 2).

Thus, our preferred interpretation for the FSVs which flow upslope, seen in the Lyot and LVSW study sites, is that they formed beneath a regionally extensive (at least tens to hundreds of kilometers across) ice cover. It is possible that some subset of the FSVs which do not flow upslope did not form beneath such a blanket; *Fassett et al*. [2010] and *Dickson et al*. [2009] have previously argued that valleys in LVSW and Lyot have formed supraglacially and proglacially during warm climate excursions, and we cannot rule out such formation processes for a subset of the valleys. If an episode of climatic warming is responsible for valley formation (see section 7.6), it is in fact very plausible that surface melt would accompany (and feed) channel formation beneath ice. However, the facts that there are no clear scaling breaks amongst the FSVs considered as a whole (e.g., Figure 8), nor a morphologically distinct type of FSV which does not flow uphill, argue against such an interpretation. Moreover, our inference of at least tens of meters of ice around many parts of both landscapes (section 7.3) suggests a continuous cover, which would not allow the recording of the surficial melt and flow processes.

A formation model featuring fill and subsequent overtopping of depressions in the landscape by water in the absence of ice cover (hypothesis 2) is not compatible with our observations. Not only does such a model struggle to explain the uphill reaches of the FSVs documented above, but we have also seen numerous examples of breaches of small basins which occur away from the lowest points on their rims (e.g., Figure 10a). This behavior is not compatible with a lake overflow model, but is characteristic of subglacial flow paths on Earth [*Shreve*, 1985]. However, we do not necessarily rule out the existence of lakes beneath the ice cover (see section 7.2).

7.2. Valley Context and Associated Features

As noted in section 3.4, both study areas contain significant accumulations of DMT with various surface textures, implying spatially variable degrees of degradation of this ice rich material [e.g., *Mangold*, 2003; *Pierce and Crown*, 2003; *Chuang and Crown*, 2005]. Crosscutting relationships—in particular showing DMT relative ages compared to the FSVs (e.g., Figures 3c, 3d, and 5b)—indicate that at least two generations of DMT are present, one preceding FSV formation (into which FSVs are sometimes cut; Figures 3c and 3d) and one postdating, or perhaps synchronous with, it (Figure 3d). This paper does not set out to disentangle this complex chronology, but we note that this multigenerational history of DMT deposition and its subsequent degradation is consistent with our model for FSV formation beneath ice cover. The scarps which form the

edges of much of the smoother surfaced, younger DMT tell us that it was once more extensive, but never do we see any evidence for the extent of this former coverage; it has left no trace on the underlying degraded DMT. It is thus not necessarily surprising that we do not see any explicit evidence for the ice cover we infer was once present over the tops of the FSVs.

It is in fact possible that this generation of DMT postdating the FSVs is the remnants of the ice cover which allowed their formation (although this could also be a later generation of ice cover regrowing over these landforms). Throughout both areas, the vast majority of eroding back DMT is not inconsistent with it being positioned stratigraphically above the FSVs, but unfortunately we have found this hypothesis stubbornly resistant to formal testing. We also infer that the controlling variable for ice preservation in the landscape is the dust or debris content of that ice [*Clow*, 1987; *Christensen*, 2003; *Bryson et al*., 2008; *Chevrier et al*., 2008; *Williams et al*., 2008; *Kowalewski et al*., 2011]. If this is the case, stripping a surface layer of cleaner ice away from a residual lag of much dirtier substrate ice to reveal the FSVs is both plausible and consistent with the known variability in the preservation potential of different exposures of DMT around these landscapes.

The ridge and mound features observed around both study sites also fit parsimoniously with a model of FSV formation beneath an ice cover. We suggest that the landform sequence FSV-ridge-mound formed at a paleomargin of the ice cover. The ridges are analogous to terrestrial eskers, which generally form as the overlying ice thins toward its margins, pressure in the pipe falls, and sediment is deposited within Röthlisberger channels cut upward into the overlying ice [*Röthlisberger*, 1972; *Walder and Fowler*, 1994]. We then interpret the mounds as landforms deposited just beyond the ice margin; these structures are significantly wider than both the upstream ridge and FSV, which argues for sudden removal of lateral constraining pressure. We tentatively envision these structures as the broad equivalent of terrestrial "aufeis," arctic environment features where liquid water escapes from an insulated and pressurized reservoir (an ice-capped stream or groundwater spring) into subzero environmental conditions and freezes into a bulbous mound of ice around the water outlet [e.g., *Kane*, 1981]. We hypothesize that the mounds would be mixtures of sediment and ice and are presumably closed systems with respect to the water and sediment fed into them (see also section 7.5). The deeply cracked and pitted surfaces of the mounds (section 3.2) are consistent with sublimation of the ice within them [*Mangold*, 2003]. It is also possible, however, that some or all of the mounds formed not at a subaerial ice margin but where the ice cover intersected a (possibly subglacial) lake and discharged sediment into it. The mounds would then form in the standing water, beneath a (frozen) lake surface, and in this model would presumably be much more sediment-rich than an aufeis-type structure, removing the requirement that they quickly freeze to retain their shape. This lake formation model is appealing as it allows us to explain more easily the mounds which form midway along a chain of FSVs, and also the mounds which form a ring around the crater in LVSW (Figure 2c, number sign). However, we also note that only in this one crater are closely spaced mounds at similar elevations, and it is also possible to argue (as we do in section 7.5) that the mounds midway along FSV chains formed during a retreat phase of the ice margins, just as moraines can form behind a terminal moraine during a glacial retreat. The aufeis model also explains the presence of the ridges more parsimoniously as pressure drop features at ice margins, and the high ice content of these features implied by the deep fissuring.

Previous authors have described these ridge-mound sequences as channel inversion features and sediment fans, respectively [*Dickson et al*., 2009; *Fassett et al*., 2010]. We do not favor this interpretation. If the ridges are inverted channels, where overbank fines have been stripped away from around an either preferentially cemented and/or significantly coarser grained central channel, then we would expect the same contrast in channel and overbank erodability to be visible in the putative downstream fans. In fact, the bodies of the mounds are strikingly homogenous and do not show evidence for strong contrasts between the channel (i.e., penetrating ridge) and the rest of the mound. This model also cannot explain the lack of distributary branching either in the mound itself or in the ridge segments, nor the distinctive convex-up, rounded in plan view morphology of the mounds, which suggest a non-Newtonian rheology at the time of deposition of this material.

7.3. How Thick Was the Ice?

Having concluded that the FSVs formed beneath a now-absent ice cover, we now aim to place constraints on the possible thicknesses of that ice. The mapping and quantitative analysis of FSVs and associated features performed here allow us to attempt this, though a full assessment of ice distribution and thickness would

require a coupled ice sheet model and is beyond the scope of this study. We also emphasize that it is very likely that the ice would have been variable in both local (thicker over local lows) and regional (thinner at the edges) thicknesses, and it is also possible that the FSVs and their associated features are a palimpsest recording differing ice thicknesses at different times (though we hypothesize that much of the FSV development seen here may correspond to a single episode of activity; see section 7.5). A single value for ice thickness is not a meaningful metric for such a landscape. With that in mind, the key constraints that our data provide are as follows:

1. The implied hydrostatic field which must have driven subglacial flow uphill probably provides the strongest constraints. Because of the large contrast between the weights of ice and air, only small surface gradients on the ice are needed to drive flow uphill against adverse topographic gradients (up to around 11 times greater), as discussed in section 4. Equivalently, this means that ice thicknesses only need to exceed the relief of the slope up which flow is being driven by a minimum of around 9% in order to satisfy the hydrostatic constraints for uphill flow. Examining the flow paths of the mapped FSVs around the two areas reveals that 20 m is a fairly typical rise against the local topographic gradient (section 7.1); channels like the one in the outer ring of Lyot with very large ($>$200 m) amplitude uphill gains (Figure 11f) are atypical. This suggests that ice thicknesses around much of the two areas must exceed 20 m over large parts of the landscapes, and locally—normally within well-defined topographic basins—must reach at least several hundreds of meters. The comparative rarity of such flows up large divides however argues that thick (more than several hundreds of meters) ice may in fact have been likewise fairly rare around the landscape.
2. Channel flow directions also provide some constraints. Although we have documented significant numbers of channels climbing over local highs, at the broadest, regional scales, the drainage patterns mapped in Figure 2 follow flow paths defined by the broad scale topography. In other words, channels in the crater interiors still flow toward the crater centers, and those outside still flow away broadly radially. No FSVs breach the outer rings of either crater. These conditions more or less rule out the possibility of completely coating the whole landscape in many kilometers of ice, such that the surfaces of the ice no longer feel the underlying topography of the craters. This conclusion is reinforced by the fact that the channel properties do show broad correlations with topographic metrics like local slope when lumped into large regional data sets (Figure 8).

Thus, we favor a typical ice thickness around these landscapes in the many tens to several hundreds of meters thickness, though we cannot absolutely rule out somewhat higher local thicknesses, especially in the crater interiors. If our "aufeis" interpretation of the ridges and mounds is correct, this also gives us snapshots of where the ice margins were at certain intervals, and those seen in the interior of LVSW argue strongly for an ice-free inner crater at the time of their formation. This would rule out truly thick (kilometer-scale) ice in the interior of LVSW. Looking at the locations of channels which do successfully climb large adverse gradients, our favored interpretation for the regional ice patterns envisions a tens of meters to hundred meters thick layer of snow and ice out on the intercrater plains, banking out to greater thicknesses against the high relief of the craters, and in the basins formed in the topography of their rims.

7.4. Hydrology

Our working hypothesis throughout this paper has been that that the two types of FSV are end-members in a single continuum of form. We interpret that discharge in the channel that cuts the FSV is the controlling variable for the resulting FSV form and type. The key distinctions between the two types in terms of increased channel width, increased meander wavelength and higher Strahler order in networks for type 2 valleys compared to type 1 would be consistent with on average higher discharges in the type 2 FSVs, were these terrestrial alluvial channels [e.g., *Knighton*, 1998, chapter 3]. We see intermediate forms, and when the data are treated as a whole we do not see differences in scaling between the two FSV forms.

The valleys in Lyot are systematically wider than those in LVSW. Valley widths should form an acceptable proxy for channel discharge (see equation (1) and section 5.1). Higher discharges in Lyot are also reflected in the relative abundances of the two types in each site (two-third type 1 in LVSW; two-third type 2 in Lyot), and the elevated valley length densities in Lyot (0.018 km^{-1} versus 0.007 km^{-1}). The consistent differences in all these parameters between sites indicate not only that the channels in the Lyot landscape systematically carried more water than those in LVSW but that the characteristics of the whole network are adapted to carry

more water. This strongly suggests that even though we have not been able to document a robust association between FSV maximum width and the catchment area sourcing it, the FSVs are not sourced from a small number of point sources. The fact that the whole network in Lyot is denser as well as the FSVs being wider argues for spatially distributed water input to the valleys.

We have argued that the FSV networks in the study areas were formed under a relatively continuous ice cover. The cover's regional extent suggests a synoptic source for the ice, i.e., atmospheric ice deposition, and the need for low permeabilities in the layer to sustain pressurized flow in the FSVs suggests snow metamorphism in the lower parts of the putative snowpack. Significant amounts of metamorphism in the snow require significant thicknesses to allow the crystallization to occur. The presence of meltwater in the snowpack may substantially aid the formation of ice; in terrestrial examples a wet snowpack may need only 10–20 m of accumulation to form dense ice at its base, a dry snowpack may need >50 m [*Paterson*, 1994], which would presumably scale to >125 m under Martian gravity. These values are consistent with our thickness estimates in section 7.3. Moreover, such thicknesses argue that this is not just seasonal snow cover, but rather that a considerable number of years of snow accumulation are required [*Clow*, 1987].

7.5. Formation Time

The formation time of the FSVs is likely to be extremely restricted. Circumstantial evidence for short formation times includes small valley incision depths, lack of inner channels in the wider type 2 FSVs, and little evidence for lateral migration in the vast majority of the FSVs, including those that tightly meander. Perhaps the strongest evidence comes from the ridge and mound structures present in both areas. If these are ice-marginal features, as in our preferred interpretation, then they are closed systems, reflecting almost the complete water and sediment budget discharged from the ice margin in that flow event (less a small fraction for sublimation of the mound after deposition). The small size of the mounds (footprint order of magnitude areas of 10^6–10^7 m^2) implies extremely restricted duration of flow for the flow producing each mound. By mass balance, we tentatively estimate this total flow timescale as ≪1 year, assuming ~10 m thick mounds and possible discharges of 10^1–10^2 m^3/s in the feeding FSVs. Such discharges are typical of FSVs with similar slopes and dimensions elsewhere on Mars [e.g., *Howard and Moore*, 2011; *Parsons et al*., 2013]—although this requires us to assume atmospheric pressure, we can justify this assumption for this calculation since the FSVs feeding the mounds are by definition ice marginal.

The lack of structure within the mounds and the small size suggest that each is probably produced by a single continuous episode of discharge. We postulate that the FSVs were cut in the same episodes as the mounds were formed, and thus on similarly restricted total timescales. We note however that where mounds are present midway along a chain of FSVs (e.g., Figures 5b, 5e, 11a, and 11c), this must imply that the mounds were deposited after much of the network was already established, and thus the total timescales for FSV formation may be somewhat longer, with the mounds being formed during a time of retreat of the ice margins. This makes sense if the formation of the FSVs and mounds is genetically linked to the rapid wasting of such an ice cover. We emphasize that the valleys upstream of the mounds do not appear in any way different from those downstream of the mounds, implying very similar flow conditions were active.

7.6. Heat Source

Several hypotheses have previously been suggested for a source of heat to initiate melting in a source ice mass to produce flow of liquid water on a relatively young Mars. Five possibilities are: melting by intense orbitally driven insolation changes under modern atmospheric conditions (increasing solar radiative flux [e.g., *Clow*, 1987; *Williams et al*., 2008]); atmospheric change resulting from impacts, volcanism, or insolation feedbacks, and associated warming (increased downwelling longwave radiation and suppressed sensible heat flux cooling the surface [e.g., *Clow*, 1987; *Kite and Manga*, 2012]); changes to geothermal fluxes by geologic change in the subsurface caused by movement of hot rock [e.g., *Gulick*, 1998, 2001; *Fassett and Head*, 2006, 2007]; catastrophic heat flux into the surface by bolide impact and its subsequent, local release [e.g., *Newsom*, 1980; *Jones et al*., 2011; *Mangold*, 2012]; and thickening of the snowpack until presumed average geothermal fluxes can melt the base under modern environmental conditions [e.g., *Carr and Head*, 2003; *Kargel et al*., 2011; *Kargel and Furfaro*, 2012].

We do not favor a mechanism based on subsurface intrusion of hot material since neither study site shows any evidence of contemporaneous igneous activity, and FSVs are present at a wide variety of longitudes at

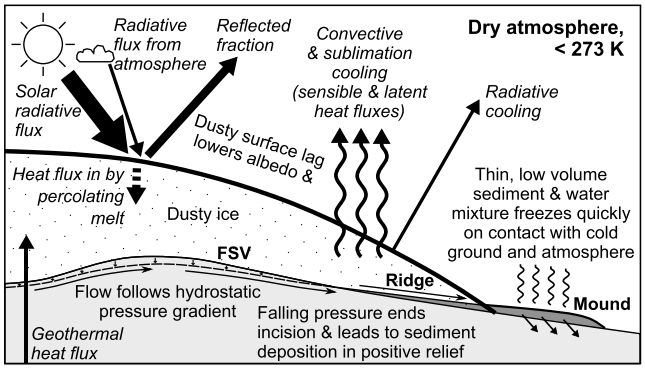

Figure 12. Schematic cartoon of hypothesized formation environment for FSVs, ridges, and mounds. Proposed heat budget fluxes governing temperature of the overlying ice mass are also shown, inferred to be governed by incoming solar radiative flux.

the global scale [*Berman et al*., 2009; *Fassett et al*., 2010], suggesting a global rather than local forcing mechanism. The statistical similarity of the derived ages of the two FSV suites (section 6.4) also argues in favor of a formation mechanism controlled by global climate change.

We can rule out a local impact heating mechanism for these two sites. While the FSVs are concentrated in the immediate vicinities of certain young craters (Lyot and the crater in LVSW (Figure 2a, number sign)), they are also present throughout the mapped areas, including 180 km from the rim of Lyot amongst the outer regions of Deuteronilus Mensae, and well outside the ejecta field of the LVSW crater (number sign), in the far south and east of that study area (Figure 2). This wide distribution is very unlikely to correspond to the effects of impact heating, which should be focused more at the crater centers and is unlikely to extend far beyond the crater rims [e.g., *Barnhart et al*., 2010]. Heating by cover with warm ballistic or fluidized ejecta is unlikely based on the distance to the outermost FSVs, the lack of any evidence for ejecta deposits in these areas, and the presence of FSVs inside craters. We have also documented a major time lag between crater formation in the Late Hesperian (LVSW) [*Fassett et al*., 2010] or Early Amazonian (Lyot) [*Dickson et al*., 2009], and FSV formation in the Late Amazonian. This definitively rules out local impact heating as the cause of FSV formation in both cases.

Ice insulation and melting by background geothermal heat is unlikely as a sole mechanism, as the required thicknesses of snow and ice appear prohibitive ($\gg$1 km [*Carr and Head*, 2003; *Kargel et al*., 2011; *Kargel and Furfaro*, 2012]) compared to our thickness estimates presented in section 7.3. Nonetheless, the insulating effect of the ice cover necessarily must play some role in the heat budget of the system. We anticipate that a climatically forced heating mechanism (Figure 12) as described above would need to be less extreme to initiate melting beneath ice cover than it would be to sustain runoff in open channels on this basis.

We believe an episode global climate change is the most parsimonious heat source (Figure 12). However, on the basis of the data presented here, it is not possible to distinguish conclusively between formation under varying orbital insolation alone, and formation under a different atmospheric environment (i.e., a greenhouse effect). The strong latitudinal banding of FSVs noted by other authors [*Berman et al*., 2009; *Fassett et al*., 2010; *Mangold*, 2012] hints at some control by insolation variation under changing obliquity, either direct or indirect. However, we have argued in section 7.5 that the formation of these two suites of FSVs appears contemporaneous and probably occurred in a single continuous episode. Likewise, very many accumulations of ice still extant on Mars (VFFs, LDM, etc.) are apparently not associated with FSVs. Together, these observations both suggest that the warming event which created these FSVs was highly atypical. Both formation during a particularly extreme orbital cycle and formation under a rare (e.g., volcanically forced) Amazonian atmospheric excursion could fulfill this requirement, as would both acting together.

8. Conclusions

Amazonian-age midlatitude valley networks have been mapped across two study sites, one in the southern highlands near Le Verrier and Kaiser craters, one in and around Lyot crater on the northern plains. We have linked this mapping to DTMs for each area in order to study quantitatively the distribution of the FSVs with

respect to local topographic slope and landscape drainage structure. Significant numbers of FSVs in both study sites cross DTM-derived basin boundaries, including some regionally significant, major drainage divides. We argue that the FSV reaches which now point upslope have not been produced by post-formation modification of the landscape and represent real instances of water flow against the topographic gradient. This demands pressurized flow beneath a cover, which we interpret to have been an overlying cap of ice and snow that has subsequently been removed from the landscape. Inferred hydrostatic heads necessary to drive uphill flow and flow paths which broadly mimic regional slopes together imply this cover remained relatively thin (many tens to several hundreds of meters thickness, though perhaps locally higher). Ridges and enigmatic mounds associated with the FSVs in both areas are consistent with eskers and ice-marginal depositional lobes, respectively. We hypothesize that the mounds form as subaerial aufeis-like freeze structures and the eskers by depressurization of subglacial conduits at the ice margins.

The rarity of abandoned valleys and small sizes of mound structures associated with the FSVs both indicate that flow was sustained for only very short timescales (perhaps of the order of days) and that flow occurred in only a very small number of events, perhaps only a single event. The distribution, locations, and formation times of the FSVs around both landscapes are inconsistent with models of formation by local impact heating. Buffered crater counting yields statistically identical, probably Late Amazonian ages for each field area. A formation mechanism involving obliquity-driven changes in insolation or global climatic warming from short-lived atmospheric changes seems likely.

Taken as a whole, the distribution of the FSVs and the ice beneath which they must have formed demands a substantial, spatially widespread—i.e., synoptic—snow/water cycle and hydrologic system active over at least some part of Late Amazonian Mars history.

Acknowledgments

The authors wish to thank David Sugden, Caleb Fassett, and Reid Parsons for insightful discussions on the material presented in this paper, and in particular Edwin Kite for both sharing thoughts on young Martian glaciofluvial environments and providing the HiRISE DTM seen in the paper. Thoughtful reviews from Olivier Bourgeois and David Crown greatly improved the presentation of the ideas in this manuscript. This work was funded by NASA grant NNX08AE47A.

References

Arfstrom, J., and W. K. Hartmann (2005), Martian flow features, moraine-like ridges, and gullies: Terrestrial analogs and interrelationships, *Icarus*, *174*(2), 321–335, doi:10.1016/j.icarus.2004.05.026.

Baker, V. R. (1981), The channels and valleys of Mars, in *Third International Colloquium on Mars*, LPI Contribution, vol. 441, pp. 12–14, Lunar and Planetary Institute, Houston, TX.

Baker, R. V., M. H. Carr, C. V. Gulick, C. R. Williams, and M. S. Marley (1992), Channels and valley networks, in *Mars*, edited by B. Kieffer et al., pp. 493–522, University of Arizona Press, Tucson.

Banks, M. E., et al. (2008), High Resolution Imaging Science Experiment (HiRISE) observations of glacial and periglacial morphologies in the circum-Argyre Planitia highlands, Mars, *J. Geophys. Res.*, *113*, E12015, doi:10.1029/2007JE002994.

Banks, M. E., N. P. Lang, J. S. Kargel, A. S. McEwen, V. R. Baker, J. A. Grant, J. D. Pelletier, and R. G. Strom (2009), An analysis of sinuous ridges in the southern Argyre Planitia, Mars using HiRISE and CTX images and MOLA data, *J. Geophys. Res.*, *114*, E09003, doi:10.1029/2008JE003244.

Barlow, N. G., and T. L. Bradley (1990), Martian impact craters: Correlations of ejecta and interior morphologies with diameter latitude, and terrain, *Icarus*, *87*, 156–179.

Barnhart, C. J., F. Nimmo, and B. J. Travis (2010), Martian post-impact hydrothermal systems incorporating freezing, *Icarus*, *208*, 101–117.

Basilevsky, A. T., S. C. Werner, G. Neukum, J. W. Head III, S. van Gasselt, K. Gwinner, and B. A. Ivanov (2006), Geologically recent tectonic, volcanic and fluvial activity on the eastern flank of Olympus Mons volcano, Mars, *Geophys. Res. Lett.*, *33*, L13201, doi:10.1029/2006GL026396.

Berman, D. C., W. K. Hartmann, D. A. Crown, and V. R. Baker (2005), The role of arcuate ridges and gullies in the degradation of craters in the Newton Basin region of Mars, *Icarus*, *178*, 465–486.

Berman, D. C., D. A. Crown, and L. F. Bleamaster (2009), Degradation of mid-latitude craters on Mars, *Icarus*, *200*(1), 77–95, doi:10.1016/j.icarus.2008.10.026.

Brass, G. W. (1980), Stability of brines on Mars, *Icarus*, *42*, 20–80.

Bryson, K. L., V. Chevrier, D. Sears, and R. Ulrich (2008), Stability of ice on Mars and the water vapor diurnal cycle: Experimental study of the sublimation of ice through a fine-grained basaltic regolith, *Icarus*, *196*, 446–458.

Burrough, P. A., and R. A. McDonell (1998), *Principles of Geographical Information Systems*, Oxford Univ. Press, New York.

Carr, M. H. (1983), Stability of streams and lakes on Mars, *Icarus*, *56*, 476–495.

Carr, M. H. (2001), Mars Global Surveyor observations of Martian fretted terrain, *J. Geophys. Res.*, *106*(E10), 23,571–23,593, doi:10.1029/2000JE001316.

Carr, M. H. (2006), *The Surface of Mars*, 2nd ed., Cambridge Univ. Press, Cambridge.

Carr, M. H., and J. W. Head III (2003), Basal melting of snow on early Mars: A possible origin of some valley networks, *Geophys. Res. Lett.*, *30*(24), 2245, doi:10.1029/2003GL018575.

Chevrier, V., D. Ostrowski, and D. Sears (2008), Experimental study of the sublimation of ice through an unconsolidated clay layer: Implications for the stability of ice on Mars and the possible diurnal variations in atmospheric water, *Icarus*, *196*(2), 459–476, doi:10.1016/j.icarus.2008.03.009.

Christensen, P. R. (2003), Formation of recent Martian gullies through melting of extensive water-rich snow deposits, *Nature*, *422*, 45–48.

Chuang, F., and D. Crown (2005), Surface characteristics and degradational history of debris aprons in the Tempe Terra/Mareotis fossae region of Mars, *Icarus*, *179*(1), 24–42, doi:10.1016/j.icarus.2005.05.014.

Clow, G. D. (1987), Generation of liquid water on Mars through the melting of a dusty snowpack, *Icarus*, *72*, 95–127.

Conway, S. J., M. P. Lamb, M. R. Balme, M. C. Towner, and J. B. Murray (2011), Enhanced runout and erosion by overland flow at low pressure and sub-freezing conditions: Experiments and application to Mars, *Icarus*, *211*(1), 443–457, doi:10.1016/j.icarus.2010.08.026.

Costard, F., F. Forget, N. Mangold, and J. P. Peulvast (2002), Formation of recent Martian debris flows by melting of near-surface ground ice at high obliquity, *Science*, *295*, 110–113.

Craddock, R. A., and A. D. Howard (2002), The case for rainfall on a warm, wet early Mars, *J. Geophys. Res.*, *107*(E11), 5111, doi:10.1029/2001JE001505.

Currier, J. H., and E. M. Schulson (1982), The tensile strength of ice as a function of grain size, *Acta Metall.*, *30*, 1511–1514.
Dickson, J. L., C. I. Fassett, and J. W. Head III (2009), Amazonian-aged fluvial valley systems in a climatic microenvironment on Mars: Melting of ice deposits on the interior of Lyot Crater, *Geophys. Res. Lett.*, *36*, L08201, doi:10.1029/2009GL037472.
Fassett, C. I., and J. W. Head III (2005), Fluvial sedimentary deposits on Mars: Ancient deltas in a crater lake in the Nili Fossae region, *Geophys. Res. Lett.*, *32*, L14201, doi:10.1029/2005GL023456.
Fassett, C. I., and J. W. Head III (2006), Valleys on Hecates Tholus, Mars: Origin by basal melting of summit snowpack, *Planet. Space Sci.*, *54*(4), 370–378, doi:10.1016/j.pss.2005.12.011.
Fassett, C. I., and J. W. Head III (2007), Valley formation on martian volcanoes in the Hesperian: Evidence for melting of summit snowpack, caldera lake formation, drainage and erosion on Ceraunius Tholus, *Icarus*, *189*(1), 118–135, doi:10.1016/j.icarus.2006.12.021.
Fassett, C. I., and J. W. Head III (2008), The timing of Martian valley network activity: Constraints from buffered crater counting, *Icarus*, *195*(1), 61–89, doi:10.1016/j.icarus.2007.12.009.
Fassett, C. I., J. L. Dickson, J. W. Head III, J. S. Levy, and D. R. Marchant (2010), Supraglacial and proglacial valleys on Amazonian Mars, *Icarus*, *208*(1), 86–100, doi:10.1016/j.icarus.2010.02.021.
Golombek, M. P., and N. T. Bridges (2000), Erosion rates on Mars and implications for climate change: Constraints from the Pathfinder landing site, *J. Geophys. Res.*, *105*(E1), 1841–1853.
Grant, J. A., and S. A. Wilson (2012), A possible synoptic source of water for alluvial fan formation in southern Margaritifer Terra, Mars, *Planet. Space Sci.*, *72*(1), 44–52, doi:10.1016/j.pss.2012.05.020.
Greeley, R., and J. E. Guest (1987), Geologic map of the eastern equatorial region of Mars, *U.S. Geol. Surv. Misc. Invest. Map*, *I-1802-B*, scale 1:15,000,000.
Gulick, V. C. (1998), Magmatic intrusions and a hydrothermal origin for fluvial valleys on Mars, *J. Geophys. Res.*, *103*(E8), 19,365–19,387.
Gulick, V. C. (2001), Origin of the valley networks on Mars: A hydrological perspective, *Geomorphology*, *37*, 241–268.
Hancock, G. S., R. S. Anderson, and K. X. Whipple (1998), Beyond power: Bedrock river incision process and form, in *Rivers Over Rock: Fluvial Processes in Bedrock Channels*, vol. 107, edited by K. J. Tinkler and E. E. Wohl, pp. 35–60, AGU Geophysical Monograph, Washington, D. C.
Harrison, T. N., M. C. Malin, K. S. Edgett, D. E. Shean, M. R. Kennedy, L. J. Lipkaman, B. A. Cantor, and L. V. Posiolova (2010), Impact-induced overland fluid flow and channelized erosion at Lyot Crater, Mars, *Geophys. Res. Lett.*, *37*, L21201, doi:10.1029/2010GL045074.
Hartmann, W. K. (2005), Martian cratering 8: Isochron refinement and the chronology of Mars, *Icarus*, *174*(2), 294–320, doi:10.1016/j.icarus.2004.11.023.
Hartmann, W. K., J. Anguita, M. A. de La Casa, D. C. Berman, and E. V. Ryan (2001), Martian cratering 7: The role of impact gardening, *Icarus*, *149*(1), 37–53, doi:10.1006/icar.2000.6532.
Head, J. W., and D. R. Marchant (2003), Cold-based mountain glaciers on Mars: Western Arsia Mons, *Geological*, *31*(7), 641–644.
Head, J. W., III, J. F. Mustard, M. A. Kreslavsky, R. E. Milliken, and D. R. Marchant (2003), Recent ice ages on Mars, *Nature*, *426*, 797–802.
Head, J. W., III, D. R. Marchant, J. L. Dickson, A. M. Kress, and D. M. H. Baker (2010), Northern mid-latitude glaciation in the Late Amazonian period of Mars: Criteria for the recognition of debris-covered glacier and valley glacier landsystem deposits, *Earth Planet. Sci. Lett.*, *294*(3-4), 306–320, doi:10.1016/j.epsl.2009.06.041.
Hecht, M. H. (2002), Metastability of liquid water on Mars, *Icarus*, *156*(2), 373–386, doi:10.1006/icar.2001.6794.
Howard, A. D. (1994), A detachment-limited model of drainage basin evolution, *Water Resour. Res.*, *30*(7), 2261–2285.
Howard, A. D., and G. Kerby (1983), Channel changes in badlands, *Geol. Soc. Am. Bull.*, *94*, 739–752.
Howard, A. D., and T. R. Knutson (1984), Sufficient conditions for river meandering: A simulation approach, *Water Resour. Res.*, *20*(11), 1659–1667.
Howard, A. D., and J. M. Moore (2011), Late Hesperian to early Amazonian midlatitude Martian valleys: Evidence from Newton and Gorgonum basins, *J. Geophys. Res.*, *116*, E05003, doi:10.1029/2010JE003782.
Howard, A. D., J. M. Moore, and R. P. Irwin III (2005), An intense terminal epoch of widespread fluvial activity on early Mars: 1. Valley network incision and associated deposits, *J. Geophys. Res.*, *110*, E12S14, doi:10.1029/2005JE002459.
Hubbard, B., R. E. Milliken, J. S. Kargel, A. Limaye, and C. Souness (2011), Geomorphological characterisation and interpretation of a mid-latitude glacier-like form: Hellas Planitia, Mars, *Icarus*, *211*(1), 330–346, doi:10.1016/j.icarus.2010.10.021.
Irwin, R. P., III, A. D. Howard, R. A. Craddock, and J. M. Moore (2005), An intense terminal epoch of widespread fluvial activity on early Mars: 2. Increased runoff and paleolake development, *J. Geophys. Res.*, *110*(E12), E12S15, doi:10.1029/2005JE002460.
Ivanov, B. A. (2001), Mars/Moon cratering rate ratio estimates, *Space Sci. Rev.*, *96*, 87–104.
Jones, A. P., A. S. McEwen, L. L. Tornabene, V. R. Baker, H. J. Melosh, and D. C. Berman (2011), A geomorphic analysis of Hale crater, Mars: The effects of impact into ice-rich crust, *Icarus*, *211*(1), 259–272, doi:10.1016/j.icarus.2010.10.014.
Kane, D. L. (1981), Physical mechanics of aufeis growth, *Can. J. Civ. Eng.*, *8*(2), 186–195.
Kargel, J. S., and R. Furfaro (2012), A frozen lake/glaciolacustrine model of crater Greg (Mars), *Lunar and Planetary Science Conference*, abstract no. 2629.
Kargel, J. S., and R. G. Strom (1992), Ancient glaciation on Mars, *Geological*, *20*, 3–7, doi:10.1130/0091-7613(1992)020<0003:agom>2.3.co2.
Kargel, J. S., V. R. Baker, J. E. Beget, J. F. Lockwood, T. L. Pewe, J. S. Shaw, and S. Robert (1995), Evidence of ancient continental glaciation in the Martian northern plains, *J. Geophys. Res.*, *100*(E3), 5351–5368.
Kargel, J. S., R. Furfaro, D. Wibben, D. C. Berman, B. Hubbard, R. E. Milliken, J. D. Pelletier, and J. A. Rodríguez (2011), Melting a Martian viscous flow feature: A modern-climate, dust-blanketed glacier model, *Lunar and Planetary Science Conference*, abstract no. 2266.
Kite, E. S., and M. Manga (2012), Seasonal snowmelt versus impact-triggered runoff in Mars' geologic record of surface liquid water, *Third Conference on Early Mars*, abstract no. 7081.
Knighton, D. (1998), *Fluvial Forms & Processes: A New Perspective*, Hodder Arnold, London.
Kowalewski, D. E., D. R. Marchant, K. M. Swanger, and J. W. Head III (2011), Modeling vapor diffusion within cold and dry supraglacial tills of Antarctica: Implications for the preservation of ancient ice, *Geomorphology*, *126*(1-2), 159–173, doi:10.1016/j.geomorph.2010.11.001.
Lange, M. A., and T. J. Ahrens (1983), The dynamic tensile strength of ice and ice-silicate mixtures, *J. Geophys. Res.*, *88*(B2), 1197–1208.
Leopold, L. B., R. A. Bagnold, M. G. Wolman, and L. M. Brush (1960), *Flow Resistance in Sinuous or Irregular Channels*, Geological Survey Professional Paper, vol. 282-D, pp. 111–134, United States Government Printing Office, Washington D. C.
Levy, J. S., and A. G. Fountain (2012), Hydrological characteristics of recurrent slope lineae on Mars based on time-resolved HiRISE analyses and comparisons with fluid flow through an Antarctic terrestrial analog regolith, *43rd Lunar and Planetary Science Conference*, *held March 19-23, 2012 at The Woodlands, Texas. LPI Contribution No. 1659, id.1029*.
Levy, J. S., J. W. Head III, and D. R. Marchant (2009), Concentric crater fill in Utopia Planitia: History and interaction between glacial "brain terrain" and periglacial mantle processes, *Icarus*, *202*, 462–476, doi:10.1016/j.icarus.2009.02.018.
Malin, M. C., and K. S. Edgett (2000), Evidence for recent groundwater seepage and surface runoff on Mars, *Science*, *288*(5475), 2330–2335, doi:10.1126/science.288.5475.2330.

Malin, M. C., and K. S. Edgett (2003), Evidence for persistent flow and aqueous sedimentation on early Mars, *Science*, *302*(5652), 1931–1934, doi:10.1126/science.1090544.
Mangold, N. (2003), Geomorphic analysis of lobate debris aprons on Mars at Mars Orbiter Camera scale: Evidence for ice sublimation initiated by fractures, *J. Geophys. Res.*, *108*(E4), 8021, doi:10.1029/2002JE001885.
Mangold, N. (2012), Fluvial landforms on fresh impact ejecta on Mars, *Planet. Space Sci.*, *62*(1), 69–85, doi:10.1016/j.pss.2011.12.009.
Marchant, D. R., and J. W. Head III (2007), Antarctic dry valleys: Microclimate zonation, variable geomorphic processes, and implications for assessing climate change on Mars, *Icarus*, *192*(1), 187–222, doi:10.1016/j.icarus.2007.06.018.
McEwen, A. S., L. Ojha, C. M. Dundas, S. S. Mattson, S. Byrne, J. J. Wray, S. C. Cull, S. L. Murchie, N. Thomas, and V. C. Gulick (2011), Seasonal flows on warm Martian slopes, *Science*, *333*(6043), 740–743, doi:10.1126/science.1204816.
Mest, S. C., D. A. Crown, and W. Harbert (2010), Watershed modeling in the Tyrrhena Terra region of Mars, *J. Geophys. Res.*, *115*, E09001, doi:10.1029/2009JE003429.
Milliken, R. E., J. F. Mustard, and D. L. Goldsby (2003), Viscous flow features on the surface of Mars: Observations from high-resolution Mars Orbiter Camera (MOC) images, *J. Geophys. Res.*, *108*(E6), 5057, doi:10.1029/2002JE002005.
Moore, J. M., A. D. Howard, R. A. Parsons, and D. E. J. Hobley (2012), Hesperian-Amazonian transition mid-latitude valleys: Markers of a late Martian climate optima?, paper presented at Division of Planetary Sciences Annual Meeting, October 14-19, Reno.
Morgan, G. A., and J. W. Head III (2009), Sinton crater, Mars: Evidence for impact into a plateau icefield and melting to produce valley networks at the Hesperian–Amazonian boundary, *Icarus*, *202*(1), 39–59, doi:10.1016/j.icarus.2009.02.025.
Morgan, G. A., J. W. Head III, and D. R. Marchant (2009), Lineated valley fill (LVF) and lobate debris aprons (LDA) in the Deuteronilus Mensae northern dichotomy boundary region, Mars: Constraints on the extent, age and episodicity of Amazonian glacial events, *Icarus*, *202*(1), 22–38, doi:10.1016/j.icarus.2009.02.017.
Mouginis-Mark, P. J. (1979), Martian fluidized crater morphology: Variations with crater size, latitude, altitude, and target material, *J. Geophys. Res.*, *84*(B14), 8011–8022.
Mustard, J. F., C. D. Cooper, and M. K. Rifkin (2001), Evidence for recent climate change on Mars from the identification of youthful near-surface ground ice, *Nature*, *412*, 411–414.
Namiki, N., and S. C. Solomon (1994), Impact crater densities on volcanoes and coronae on Venus: Implications for volcanic resurfacing, *Science*, *265*, 929–933.
Neukum, G., R. Jaumann, T. H. Co-Investigator, and E. Team (2012), HRSC: The High Resolution Stereo Camera of Mars Express, in *Mars Express: The Scientific Payload*, vol. ESA SP-1240, edited by A. Wilson, pp. 17–35, ESA Publications Division, Noordwijk, Netherlands.
Newsom, H. E. (1980), Hydrothermal alteration of impact melt sheets with implications for Mars, *Icarus*, *44*, 207–216.
Parsons, R. A., J. M. Moore, and A. D. Howard (2013), Evidence for a short period of hydrologic activity in Newton crater, Mars, near the Hesperian-Amazonian transition, *J. Geophys. Res. Planets*, *118*, 1082–1093, doi:10.1002/jgre.20088.
Paterson, W. S. (1994), *The Physics of Glaciers*, Pergamon, Tarrytown, NY.
Phillips, R. J., et al. (2001), Ancient geodynamics and global-scale hydrology on Mars, *Science*, *291*, 2587–2591, doi:10.1126/science.1058701.
Pierce, T. L., and D. A. Crown (2003), Morphologic and topographic analyses of debris aprons in the eastern Hellas region, Mars, *Icarus*, *163*(1), 46–65, doi:10.1016/S0019-1035(03)00046-0.
Pieri, D. C. (1980), Martian valleys: Morphology, distribution, Age, and origin, *Science*, *210*(4472), 895–897, doi:10.1126/science.210.4472.895.
Röthlisberger, H. (1972), Water pressure in intra- and subglacial channels, *J. Glaciol.*, *11*, 177–203.
Schon, S. C., and J. W. Head III (2011), Keys to gully formation processes on Mars: Relation to climate cycles and sources of meltwater, *Icarus*, *213*(1), 428–432, doi:10.1016/j.icarus.2011.02.020.
Sharp, R. P., and M. C. Malin (1975), Channels on Mars, *Geol. Soc. Am. Bull.*, *86*(5), 593–609.
Shreve, R. L. (1972), Movement of water in glaciers, *J. Glaciol.*, *11*(62), 205–214.
Shreve, R. L. (1985), Esker characteristics in terms of glacier physics, Katahdin esker system, Maine, *Geol. Soc. Am. Bull.*, *96*, 639–646, doi:10.1130/0016-7606(1985)96<639:ecitog>2.0.co2.
Squyres, S. W. (1979), The distribution of lobate debris aprons and similar flows on Mars, *J. Geophys. Res.*, *84*, 8087–8096.
Squyres, S. W., and M. H. Carr (1986), Geomorphic evidence for the distribution of ground ice on Mars, *Science*, *231*, 249–252.
Sugden, D. E., and B. S. John (1976), *Glaciers and Landscape: A Geomorphological Approach*, Edward Arnold, London.
Tanaka, K. L. (1982), A new time-saving crater-count technique with application to narrow features, NASA Tech. Memo., no. 85127, pp. 123–125.
Tanaka, K. L., J. A. Skinner Jr., and T. M. Hare (2005), Geologic map of the northern plains of Mars, Scientific Investigations Map 2888, U.S. Geological Survey, scale 1:15,000,000-1:7,500,000.
Tribe, A. (1992), Automated recognition of valley lines and drainage networks from grid digital elevation models: A review and a new method, *J. Hydrol.*, *139*(1-4), 263–293, doi:10.1016/0022-1694(92)90206-B.
Walder, J. S., and A. Fowler (1994), Channelized subglacial drainage over a deformable bed, *J. Glaciol.*, *40*(134), 3–15.
Wallace, D., and C. Sagan (1979), Evaporation of ice in planetary atmospheres: Ice-covered rivers on Mars, *Icarus*, *39*, 385–400.
Werner, S. C., and K. L. Tanaka (2011), Redefinition of the crater-density and absolute-age boundaries for the chronostratigraphic system of Mars, *Icarus*, *215*(2), 603–607, doi:10.1016/j.icarus.2011.07.024.
Whipple, K. X., and G. E. Tucker (1999), Dynamics of the stream-power river incision model: Implications for height limits of mountain ranges, landscape response timescales and research needs, *J. Geophys. Res.*, *104*, 17,661–17,674.
Wichman, R. W., and P. H. Schultz (1989), Sequence and mechanisms of deformation around the Hellas and Isidis impact basins on Mars, *J. Geophys. Res.*, *94*(B12), 17,333–17,357.
Williams, K. E., O. B. Toon, J. L. Heldmann, C. P. McKay, and M. T. Mellon (2008), Stability of mid-latitude snowpacks on Mars, *Icarus*, *196*(2), 565–577, doi:10.1016/j.icarus.2008.03.017.
Zuber, M. T., D. E. Smith, S. C. Solomon, D. O. Muhleman, J. W. Head III, J. B. Garvin, J. B. Abshire, and J. L. Bufton (1992), The Mars Observer Laser Altimeter investigation, *J. Geophys. Res.*, *97*(E5), 7781–7797.